Department of Physics and Astronomy

Heidelberg University

Master thesis

in Physics

submitted by

Stefan Blenkle

born in Donaueschingen (Germany)

2023

Measurement of the branching fraction of $D^0 \to K^-\pi^+e^-e^+$ with the LHCb experiment

This Master thesis has been carried out by Stefan Blenkle

at the

Physikalisches Institut Heidelberg

under the supervision of

Prof. Dr. Ulrich Uwer

Zusammenfassung:

In dieser Arbeit wird die Messung des Verzweigungsverhältnisses des Vierkörperzerfalls $D^0 \to K^-\pi^+e^-e^+$ vorgestellt. Die für die Analyse verwendeten Daten wurden in den Jahren 2017 und 2018 vom LHCb-Experiment in Proton-Proton-Kollisionen am Large Hadron Collider (LHC) aufgenommen. Es werden Zerfallskandidaten mit Dielektronenmassen im Bereich von 675 bis 875 MeV/c^2 betrachtet. Die Messung wird relativ zum Normalisierungskanal $D^0 \to K^-\pi^+\pi^-\pi^+$ durchgeführt. Der resultierende Wert für das Verzweigungsverhältnis ist:

$$\mathcal{B}_{D^0\to K^-\pi^+[e^-e^+]_{\rho^0,\omega}} = (3.6 \pm 0.2(\text{stat.}) \pm 0,7(\text{sys.}) \pm 0,06) \times 10^{-6}, \qquad (0.1)$$

wobei die Unsicherheiten statistisch, systematisch und durch die Unsicherheit des Verzweigungsverhältnisses des Normalisierungskanals $D^0 \to K^-\pi^+\pi^-\pi^+$ bedingt sind. Das Ergebnis stimmt mit der früheren Messung der BaBar-Kollaboration überein.

Abstract:

This thesis presents the branching fraction measurement of the four-body decay $D^0 \to K^-\pi^+e^-e^+$. The dataset used for the analysis was collected in 2017 and 2018 by the LHCb experiment in proton-proton collisions at the Large Hadron Collider (LHC). Decay candidates with dielectron masses in the range of 675 to 875 MeV/c^2 are considered. The measurement is performed relative to the normalization channel $D^0 \to K^-\pi^+\pi^-\pi^+$. The resulting value for the branching fraction is:

$$\mathcal{B}_{D^0\to K^-\pi^+[e^-e^+]_{\rho^0,\omega}} = (3.6 \pm 0.2(\text{stat.}) \pm 0.7(\text{sys.}) \pm 0.06) \times 10^{-6}, \qquad (0.2)$$

where the uncertainties are statistical, systematic and due to the uncertainty of the branching fraction of the normalization channel $D^0 \to K^-\pi^+\pi^-\pi^+$, respectively. The result is consistent with the previous measurement by the BaBar collaboration.

Contents

1 Introduction

The goal of particle physics is to understand the fundamental building blocks of our universe and the interactions between them. Our current knowledge in this field is condensed in the Standard Model of particle physics. The story of the Standard Model began in the 1960s and 70s, the last missing fundamental particle, the Higgs boson, was found in 2012 by ATLAS [1] and CMS [2]. Many precise predictions of the Standard Model were confirmed by experimental data in the last decades. Despite its great success, open questions, that the Standard Model is not able to answer, remain: What is Dark Matter and how do Dark Matter particles interact with Standard Model particles? What is the explanation to the observed matter-antimatter asymmetry? How can gravity be combined with the Standard Model? To be able to answer these questions, it is necessary to know where the predictions of the Standard Model differ from experimental data to receive insights on how the model has to be extended. Therefore, the focus of modern particle physics lies on testing the Standard Model and discovering new physics effects beyond the Standard Model. This is done either by directly searching for new, unknown particles or by finding discrepancies between theory and data.

One way to probe new physics phenomena is to analyze rare charm decays [1] of the form $D^0 \to h^+h^-\ell^+\ell^-$, where a D^0 meson decays into two oppositely charged hadrons ($h = \pi, K$) and two oppositely charged leptons ($\ell = e, \mu$). These decays proceed either through an intermediate meson resonance or feature a flavor-changing neutral current (FCNC) [3]. In the Standard Model, FCNC processes can not occur at tree level and are therefore suppressed. New physics processes, however, could enhance the FCNC contributions. Thus, rare charm decays are promising candidates for discovering new physics effects. The LHCb experiment at the Large Hadron Collider (LHC) is especially suitable for studying these decays as it currently has the world's largest charm dataset. In recent years, the D^0 decays into two hadrons and two muons, $D^0 \to K^+K^-\mu^+\mu^-$ and $D^0 \to \pi^+\pi^-\mu^+\mu^-$, were measured and analyzed by the LHCb collaboration [4, 5]. Tests of lepton flavor universality could follow by investigating the decays with two electrons instead of two muons in the final state. It is expected that LHCb will reach sensitivities high enough to be able to observe these decay modes in the near future [6]. In contrast to $D^0 \to h^+h^-e^+e^-$ decays, the decay $D^0 \to K^-\pi^+e^-e^+$ is less suppressed while having a similar decay topology. Therefore, it presents a suitable reference channel for the upcoming $D^0 \to h^+h^-e^+e^-$ decay searches.

[1] Unless stated otherwise, charge conjugation is implied throughout this thesis

In this thesis, the branching fraction of $D^0 \to K^-\pi^+e^-e^+$ is determined for decays with dielectron masses in the kinematic range from 675 to 875 MeV/c^2. In this region, the decay is used as normalization channel. Decay candidates are expected to be dominated by intermediate resonances of ρ^0 and ω mesons (see chapter 2). The analogous decay with two final state muons, $D^0 \to K^-\pi^+\mu^+\mu^-$, has already been measured by the LHCb collaboration [7]. The measurement was performed for dimuons in the same kinematic mass range. As the non-resonant contributions to these decays do not require FCNCs, no new physics is expected. However, both decays could still be compaired to test lepton flavor universality; apart from phase space differences due to the different masses of the leptons, both decays are predicted to be equal.

This thesis is structured as follows: In the next chapter, the Standard Model of particle physics is briefly introduced, followed by the theoretical background of the studied processes. Chapter 3 gives an overview of the LHC and the LHCb experiment. The analysis strategy, as well as the tools used in the analysis are presented in chapter 4. The event selection is explained in chapter 5. Chapter 6 describes the fitting procedure used to determine event yields. The reconstruction and selection efficiencies are determined in chapter 7. In chapter 8, the major systematic uncertainties of the measurement are evaluated. The final result is presented in chapter 9 followed by a discussion and conclusion in chapter 10.

2 Theory

This chapter briefly introduces the Standard Model of particle physics which is the theoretical foundation for describing meson decays. The second section describes the studied decay $D^0 \to K^-\pi^+e^-e^+$. A more detailed description of the Standard Model can be found in [8].

2.1 The Standard Model

The Standard Model (SM) of particle physics describes the fundamental particles that make up our universe and their interactions. It covers three of the four known fundamental forces: The electromagnetic force, the strong force and the weak force. One quantity that dictates the behaviour of particles is their spin. Particles with half-integer spin are called fermions. They obey the rules of Fermi-Dirac statistics and they cannot be in the same quantum state due to the Pauli exclusion principle. On the other hand, particles carrying integer spin are called bosons and they obey the rules of Bose-Einstein statistics.

In the SM, all known matter consists of fermions while the bosons are force carriers in interactions between particles. There are two types of fermions: The quarks and the leptons. Each of these groups consists of 6 particles. The quarks can be further subdivided into three generations with one up-type quark (u, c, t) and one down-type quark (d, s, b) each. Up-type quarks carry an electric charge of $\frac{2}{3}$, whereas down-type quarks carry an electric charge of $-\frac{1}{3}$. The leptons are also ordered in three generations of one electrically charged lepton (e^-, μ^-, τ^-) which carries an electric charge of -1 and one uncharged neutrino $(\nu_e, \nu_\mu, \nu_\tau)$. For each of these particles exists a corresponding antiparticle carrying the inverted charge. The boson content of the SM consists of four types of gauge bosons (gluons, photon, Z^0 boson, W bosons) and the Higgs boson. The particle content of the SM is summarized in figure 2.1.

All interactions in the SM can be described by the Lagrangian. It is locally gauge invariant under the $SU(2)_L \times U(1)_Y \times SU(3)_C$ symmetry group. This means that according to Noether's theorem [10], there is a conserved charge for each interaction corresponding to the symmetries.

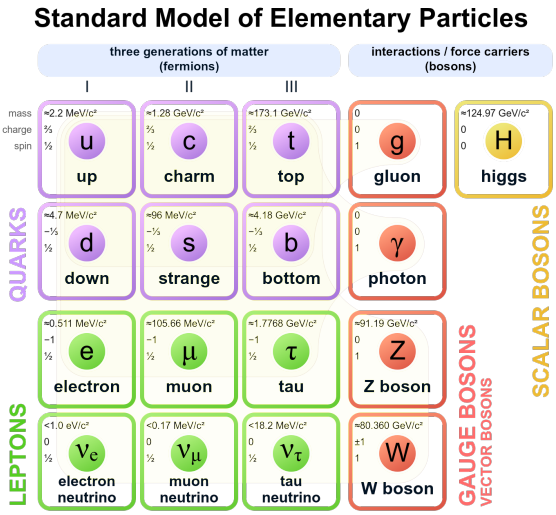

Figure 2.1: The Standard Model of elementary particles.[9]

2.1.1 Quantum Chromo Dynamics

Quantum Chromo Dynamics (QCD) is the quantum field theory describing the strong interaction generated by the $SU(3)_C$ symmetry. Eight massless gauge bosons, the so-called gluons, aswell as the quarks carry the conserved charge of this interaction, the so-called color charge (red, green, blue). Only quarks and gluons interact strong. The gluons themselves can also couple to each other resulting in gluon-gluon interactions. This is why at large distances or small momentum transfers the coupling strength α_S decreases leading to the concept called *color confinement*. It states that colored objects cannot propagate freely which means that quarks are confined to colorless bound states, the so-called hadrons. There are hadrons consisting of a quark-antiquark pair, where the antiquark carries the anticolor of the quark, called mesons, and baryons, which consist of three quarks where all three colors are present. Also, more exotic bound states of four or five quarks (tetraquark or pentaquark) are possible and are subjects of recent and ongoing studies and searches [11, 12]. Qualitatively, one can understand color confinement by imagining two quarks that are pulled apart: The quarks interact with each other by exchanging virtual gluons which also interact with themselves as a result of being color charged aswell. Therefore, as the distance between the quarks grows larger, the color field between them gets squeezed into a tube-like shape. This results in the energy density of the field being constant and the energy stored in the field grows with the separation of the quarks. Eventually, it is energetically more favourable to create a new quark pair in the middle thus making it impossible to separate the quarks completely. Nevertheless, at large momentum transfers or small distances, quarks and gluons can be treated as free particles as the coupling becomes small. This is called *asymptotic freedom*.

2.1.2 Electroweak Interaction

The electroweak interaction is a result of the $SU(2)_L \times U(1)_Y$ symmetry of the Lagrangian. It combines the electromagnetic and weak interaction. The affiliated gauge bosons are W^1, W^2 and W^3 for the $SU(2)_L$ part and B for the $U(1)_Y$ part. They couple to the weak isospin and the hypercharge, respectively. Only the left-handed fermions have weak isospin $\frac{1}{2}$ and form isospin doublets, while right-handed fermions don't carry weak isospin and cannot couple to the W^i bosons. Therefore, only left-handed particles or right-handed antiparticles can interact via the $SU(2)_L$ part of the electroweak force. In contrast to that, all fermions can couple to the B gauge boson. The $SU(2)_L \times U(1)_Y$ symmetry is spontaneously broken through the Higgs-mechanism. By introducing an addidional scalar field, the Higgs field, the four gauge bosons of the electroweak interactions are mixed into two charged W^+ and W^- bosons, the Z^0 boson and the photon (γ). It is also through this mechanism that the carriers of the weak force, the $W^\pm$ and the Z^0, become massive while the photon, that carries the electromagnetic force, remains massless. Furthermore, all massive fermions aquire their mass by their Yukawa-couplings to the massive Higgs boson.

In the SM, the only way to change flavor is by exchanging a $W^\pm$ in so-called weak charged current interactions. For example, one way to change from an up-type quark q to a down-type quark q' is by producing a W^+: $q \to q'W^+$. The corresponding amplitude of the interaction can be calculated by using the corresponding matrix element $V^*_{qq'}$ of the Cabibbo-Kobayashi-Maskawa (CKM) matrix [13]. The CKM matrix is a unitary, complex 3×3 matrix. Through the unitarity condition and absorbing unphysical phases into the quark fields, the 18 free parameters reduce to four which can be split into three Euler angles and one phase. Another way of writing the CKM matrix, that highlights its almost diagonal structure, is the Wolfenstein parametrisation [14]:

$$V_{CKM} = \begin{pmatrix} V_{ud} & V_{us} & V_{ub} \\ V_{cd} & V_{cs} & V_{cb} \\ V_{td} & V_{ts} & V_{tb} \end{pmatrix} = \begin{pmatrix} 1 - \frac{1}{2}\lambda^2 & \lambda & A\lambda^3(\rho - i\eta) \\ -\lambda & 1 - \frac{1}{2}\lambda^2 & A\lambda^2 \\ A\lambda^3(1 - \rho - i\eta) & -A\lambda^2 & 1 \end{pmatrix} + \mathcal{O}(\lambda^4) \tag{2.1}$$

with the Wolfenstein parameters $\lambda \approx 0.23$, $A \approx 0.83$, $\rho \approx 16$ and $\eta \approx 0.35$. This structure shows that transitions within the same generation are favoured while transitions between different generations are suppressed by powers of λ.

2.2 Charm Decays

The charm system has a unique position among heavy mesons, because it is the only way to probe decays of up-type quarks in mesons. This is the case since top quarks are too heavy to be able to hadronize and have a short lifetime.

This thesis focuses on the rare four-body decay $D^0 \to K^-\pi^+e^-e^+$. It is part of the semileptonic decay modes of the D^0, which are less prominent as the D^0 more frequently decays into purely hadronic final states involving pions and kaons. When looking at the quark content of the initial state meson ($|D^0\rangle = |c\bar{u}\rangle$) and the final state mesons ($|K^-\rangle = |s\bar{u}\rangle$, $|\pi^+\rangle = |u\bar{d}\rangle$), the decay involves a $|\Delta C| = 1$ transition, where C is the number of charm quarks. This means, it involves quark flavour changes that are mediated by the weak force. By looking at the corresponding CKM matrix elements, the decay $D^0 \to K^-\pi^+e^-e^+$ is favoured compared to the decay, where the charges of the kaon and pion are swapped ($D^0 \to K^+\pi^-e^+e^-$). The total branching fraction for this decay is estimated to be in the order of 10^{-6} [15].

However, the theoretical prediction is very difficult, as there are a number of ways how the D^0 can decay into the signal channel. A very simple Feynman diagram of the decay is given in figure 2.2a. In this process, a photon is radiated away and produces a pair of electrons. Kinematically, the two electrons are allowed to have a whole range of momentum values. However, a very dominant contribution is expected to come from decays where the e^+e^--pair is produced via intermediate $q\bar{q}$-resonances. The corresponding Feynman diagram is given in figure 2.2b. The two resonant states, that are important for this decay, are the ρ^0 and ω resonances. The ρ^0 meson has a mass of about $775\,\mathrm{MeV}/c^2$ and carries spin 1. Together with the ρ^+ and ρ^- it forms an isospin triplet. The quark content of the ρ^0 meson is described by a mixture of $|u\bar{u}\rangle$ and $|d\bar{d}\rangle$: $|\rho^0\rangle = \frac{1}{\sqrt{2}}(|u\bar{u}\rangle - |d\bar{d}\rangle)$. The ω meson has a mass of about $783\,\mathrm{MeV}/c^2$ and also carries spin 1. Compared to the ρ mesons, its flavor wave-function is anti-symmetric and it is an isospin singlet. The quark content of the ω meson is also described by a mixture of $|u\bar{u}\rangle$ and $|d\bar{d}\rangle$: $|\rho^0\rangle = \frac{1}{\sqrt{2}}(|u\bar{u}\rangle + |d\bar{d}\rangle)$.

The dominant contribution of these two resonances is visible when looking at the decay width as a function of the squared dielectron mass m^2_{ee} shown in figure 2.3. In the region where the invariant mass of the two electrons is in the mass range of the ρ^0 or ω meson ($m^2_{ee} \approx 0.6(\,\mathrm{GeV}/c^2)^2$, corresponding to $m_{ee} \approx 775\,\mathrm{MeV}/c^2$), the decay width is significantly enhanced. Therefore, a useful approach to perform a first observation study of the decay $D^0 \to K^-\pi^+e^-e^+$ is to restrict the dielectron mass to lie in a window around these resonances. This should maximize the signal to background ratio.

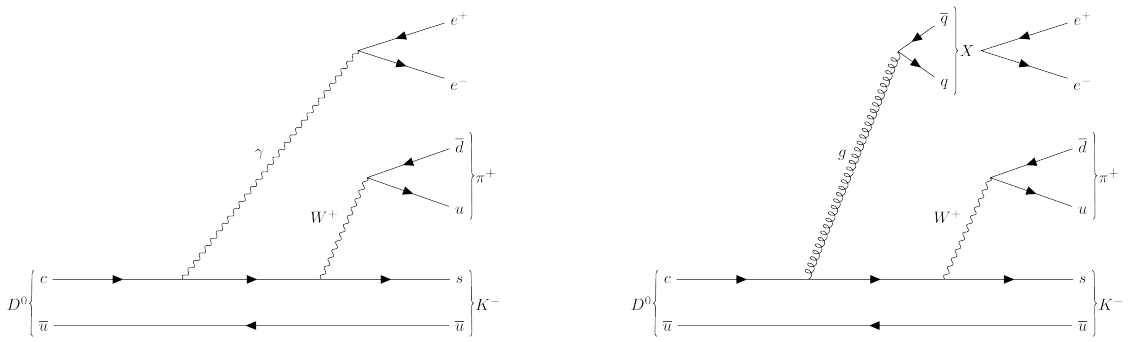

Figure 2.2: Possible Feynman diagrams for the decay $D^0 \to K^-\pi^+e^-e^+$. In the left diagram, the electron pair is produced from a radiated photon, in the right diagram it is produced by an intermediate $q\bar{q}$-resonance X.

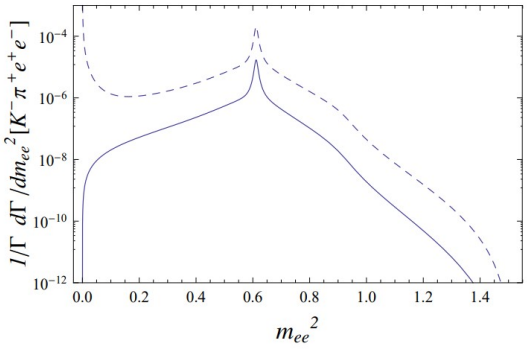

Figure 2.3: Differential decay width as a function of m_{ee}^2 (in $(\,\mathrm{GeV}/c^2)^2$) normalized to the total decay width. The dashed line corresponds to the differential decay width. [15]

The first measurement of the decay $D^0 \to K^-\pi^+e^-e^+$ was performed by the BaBar collaboration for the dielectron mass in the range of 675 to 875 MeV/c^2 [16]. They used e^+e^- collision data corresponding to an integrated luminosity of 468 fb^{-1}. The measurement was performed relative to the decay $D^0 \to K^-\pi^+\pi^-\pi^+$. The branching fraction was determined to be:

$$\mathcal{B}_{D^0\to K^-\pi^+e^-e^+} = (4.0 \pm 0.5 \pm 0.2 \pm 0.1) \times 10^{-6}, \tag{2.2}$$

where the first uncertainty is statistical, the second is systematic and the third is due to the uncertainty of the branching fraction of the normalization channel. The aim of this thesis is to do an improved measurement using the data sample acquired by the LHCb experiment. The measurement of decays involving electrons is challenging at LHCb. Due to the high center of mass energy of the proton-proton collision, a large amount of light final state particles, such as pions and electrons,

are produced, leading to a high background contamination. Additionally, the LHC provides high collision rates. This increases the difficulty of vertex reconstruction and electron identification compared to experiments at electron-positron colliders such as BaBar.

In this analysis, decay candidates from $D^0 \to K^-\pi^+e^-e^+$ decays and the corresponding charge conjugated $\bar{D}^0 \to K^+\pi^-e^+e^-$ decays are used. The D^0 meson candidates are taken from decays of $D^{*\pm}(2010)$[1] mesons into a neutral D meson and a charged pion. The corresponding Feynman diagrams are given in figure 2.4. The decays are mediated by the strong force, which conserves the flavor of the c-quark. Therefore, the charge of the pion indicates the quark content of the neutral D meson: A π^+ corresponds to a D^0 meson and a π^- to a $\bar{D}^0$ meson, respectively. These decays are referred to as *prompt* decays, as the lifetime of the $D^{*\pm}$ meson is less than $10^{-20}\,\mathrm{s}$ because of the strong decay. The production and decay vertex of the $D^{*\pm}$ meson are experimentally not separable. Furthermore, the mass difference between the $D^{*\pm}$ and its decay daughters is about $6\,\mathrm{MeV}/c^2$. This leads to the pion having a small momentum compared to the neutral D meson [3]. In the following, the pion produced in the prompt $D^{*\pm} \to D\pi^\pm$ decay is referred to as slow pion π_s. Additionally, the mass difference between the $D^{*\pm}$ and neutral D mesons presents an excellent selection quantity against background candidates as it lies in a tight window around the pion mass.

The measurement presented in this thesis is performed relative to the decay $D^0 \to K^-\pi^+\pi^-\pi^+$. Decay candidates are selected from prompt $D^{*\pm}$ decays. Additionally, the decay with oppositely charged kaon and first pion can occur. In contrast, this decay is suppressed due to off-diagonal CKM matrix elements. In this thesis, $D^0 \to K^-\pi^+\pi^-\pi^+$ and $D^0 \to K^+\pi^-\pi^+\pi^-$ decays are referred to as right-sign and wrong-sign decays, respectively. The charge of the slow pion in the prompt decay is used to separate right-sign and wrong-sign candidates. In the analysis, the wrong-sign decays are used in background studies.

Charged particles that traverse through matter can loose energy by emitting photons in interactions with nuclei. This process is called bremsstrahlung. The rate R of these processes depends on the mass m of the particle: $R \propto \frac{1}{m^2}$ [8]. Therefore, bremsstrahlung is particularly emitted by electrons.

[1] In the following referred to as $D^{*\pm}$

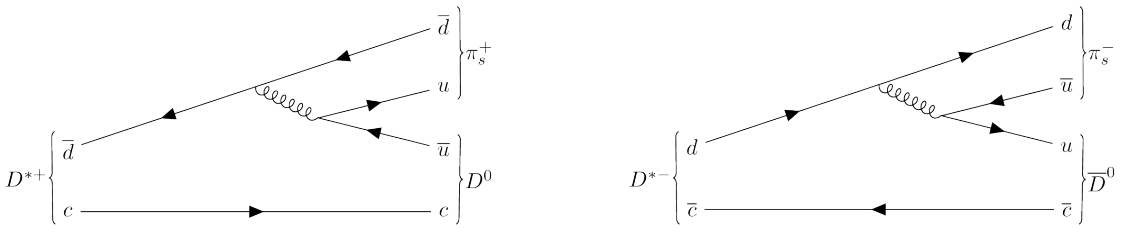

Figure 2.4: Feynman diagrams for the strong decays $D^{*+} \to D^0\pi^+$ (left) and $D^{*-} \to \bar{D}^0\pi^-$ (right). The subscript s refers to the small momentum of the pion.

3 The LHCb Experiment

This chapter gives an overview of the LHCb detector at the Large Hadron Collider. The focus lies on the sub-detectors relevant for the branching fraction measurement of $D^0 \to K^-\pi^+e^-e^+$.

3.1 The Large Hadron Collider

Situated at the European Organization for Nuclear Research (CERN), the Large Hadron Collider (LHC) [17] is the largest circular accelerator to date. It is located in a tunnel with a circumference of 27 km under the French Swiss border. Protons or heavy ions injected from a pre-accelerator complex are accelerated close to the speed of light and stored in two opposing high energy particle beams. Superconducting magnets are used to keep the particles on a circular orbit. The beams collide in four collision points where the four main experiments, CMS, ATLAS, ALICE and LHCb are located. ATLAS and CMS are designed as general-purpose detectors for the search of the Higgs and direct hints for beyond Standard Model physics. The ALICE experiment is dedicated to study heavy ion collisions. The LHCb experiment is specialized for studying the properties and decays of hadrons containing c and b quarks. The time periods when collisions take place at the LHC and the experiments take data are referred to as Runs. In between two Runs there is a shutdown phase in which the LHC itself and the experiments are maintained and upgraded. During Run 1, which took place from 2009 to 2012, the LHC collided protons at a center-of-mass energy of $\sqrt{s} = 7\,\text{TeV}$ and $\sqrt{s} = 8\,\text{TeV}$. After the first long shutdown, data taking was resumed in Run 2 between 2015-2018 and a center-of-mass energy of 13 TeV was reached. Further upgrades to reach higher luminosities were installed during the second shutdown. At the time of this thesis, a third run period, which started in 2022, is ongoing.

3.2 The LHCb Detector

The LHCb detector [18] is one of the four large experiments at the LHC and is specially designed for studying b and c flavoured hadrons. As heavy quarks are mainly produced in the forward direction with respect to the beam, LHCb is build as a single-arm forward facing spectrometer. It covers an angle with respect to the beamline of approximately 10 to 300 (250) mrad in the x-z (y-z) plane. The right-handed coordinate system of the detector is defined with the beam-line along the z-direction and the y-axis pointing upwards. The detector layout with all the

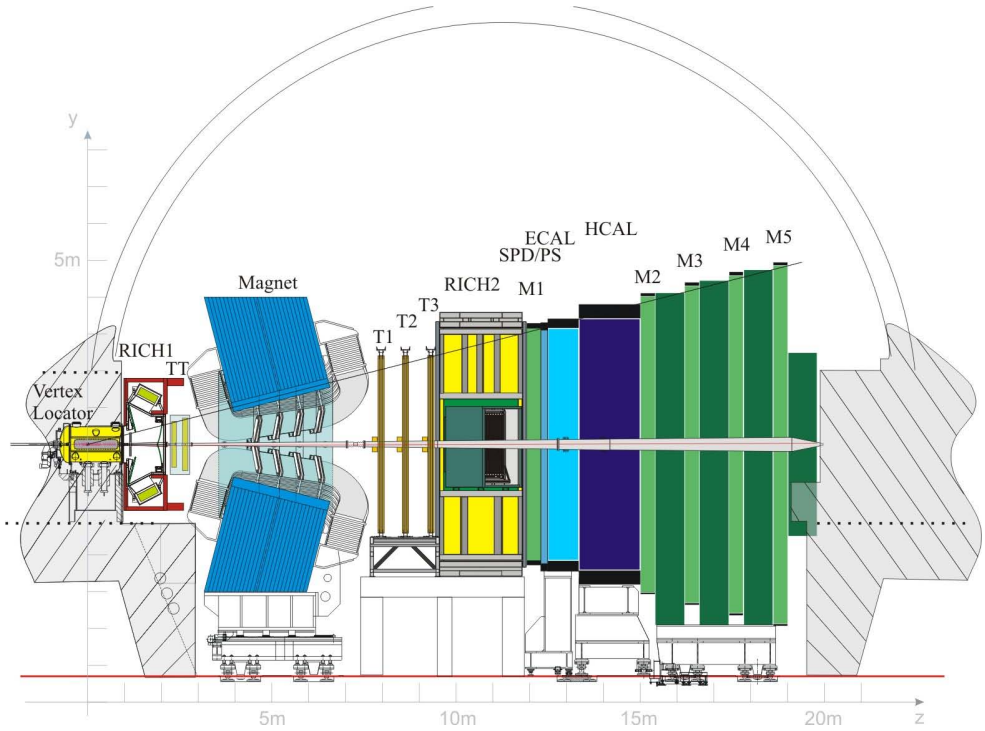

Figure 3.1: LHCb detector layout for Run 1 and 2. [19]

sub-detectors is shown in figure 3.1.

In the following sections, the individual parts of the detector are explained.

3.2.1 Vertex Locator

The Vertex Locator (VELO) is placed around the proton-proton collision point to accurately determine primary and secondary vertices of measured tracks. It consists of silicon strip modules measuring radius r and angle ϕ of the particles. The z-component is determined by the position of the sensor. With this, the VELO can determine decay lengths of long-lived particles by using the primary and secondary vertices. From the decay lengths, the corresponding live times can then be derived. Additionally, the VELO is able to precisely determine impact parameters of particle tracks. The impact parameter (IP) is defined as the minimal distance of the track to the primary vertex. It can be used to select particles coming from secondary decay vertices.

During data taking, there is only a gap of 7 mm between the beam and the VELO. However, to prevent damage during the injection time of the beam, the sensors have to be further away. This is why the VELO is composed of two movable halves. Only when the beam is stable, they are moved into the closed position (see figure 3.2).

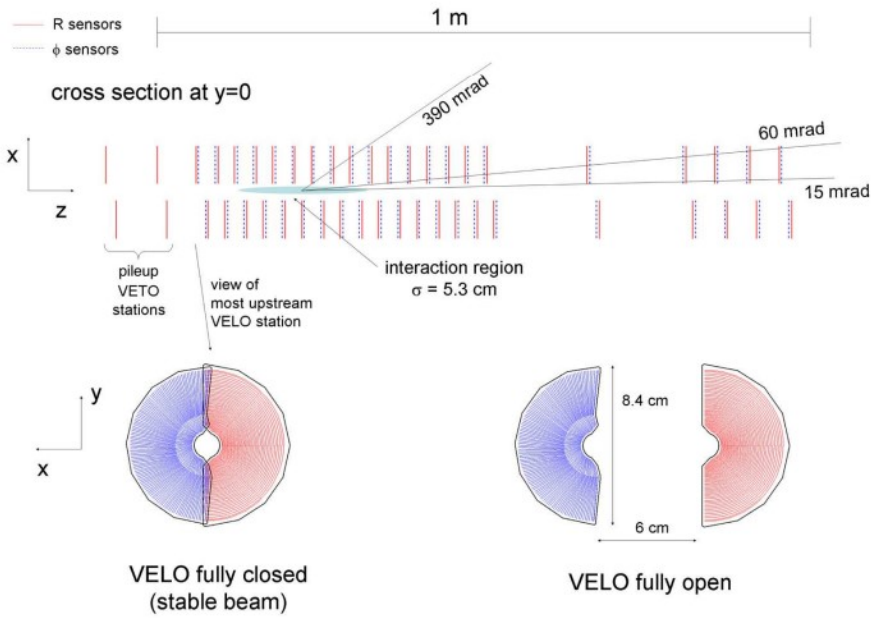

Figure 3.2: Layout of the Vertex Locator. At the top, the placement of the modules along the beam axis is shown. The two figures at the bottom illustrate the closed and open positions of a pair of modules. [18]

3.2.2 Magnet

Charged particles that move through a magnetic field are affected by the Lorentz force, which bends their path. The curvature of the path depends on the magnetic field strength and direction relative to the path, the charge and the momentum of the particle. This in turn provides a method to measure the momentum of a particle by determining the curvature of its path. A large dipole magnet is used to supply the magnetic field. It consists of two identical, saddle-shaped aluminium coils mounted inside a steel yoke. The coils are made up of fifteen pancake-like layers arranged in five triplets. The magnetic field is mostly aligned with the y-axis and has an integrated strength of 4 Tm for particles traversing the whole detector. The polarity of the magnet is regularly flipped due to asymmetries in the detector. The polarities are called *magnet up* (MagUp) and *magnet down* (MagDown) corresponding to the magnetic field pointing along the positive or negative y-axis, respectively.

3.2.3 Tracking Stations

The tracking stations of the LHCb tracking system are located next to the magnet. The Tracker Turicensis (TT) is before and T1-T3 are after the magnet. The TT consists of silicon micro strip detectors arranged in two stations with four layers each. The outer two layers are oriented vertically whereas the inner two layers are rotated by an angle of $\pm 5^\circ$. This provides additional information on the y-coordinate

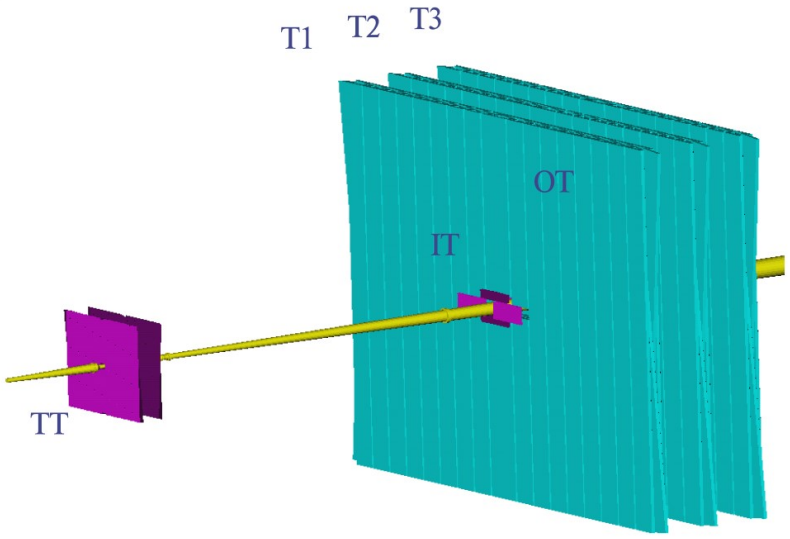

Figure 3.3: The LHCb tracking system [20]. The Inner Tracker (IT) of the main tracking stations (T1-T3) and the Tracker Turicensis (TT) consists of silicon detectors (marked in purple). The drift-time detector of the outer tracker (OT) is marked in cyan.

of the tracks. The main tracking stations T1-T3 are also made of four layers each. However, each layer combines two distinct detector technologies: The Inner Tracker (IT) is located in the innermost regions close to the beam pipe, where the occupancy of tracks is significantly higher than in the outer regions, that are covered by the Outer Tracker (OT), as shown in figure 3.3. Similar to the TT, the IT uses silicon micro strip detectors. Both detectors, TT and IT, reach a spatial hit resolution of 50 µm in x. The OT is a drift-time detector consisting of gas-filled straw tubes. Like for the TT, the inner two layers of the tracking stations T1-T3 are rotated by an angle of $\pm 5°$, which allows for a measurement of the y-coordinate. Due to their spatial arrangement, the tracking stations reach a higher resolution in the x-direction than in the y-direction. This choice was made by design, the x-variable is more important for track reconstruction, since the paths of charged particles are bent in the x-direction by the vertical magnetic field.

3.2.4 Ring-Imaging Cherenkov Detectors

To study decay processes in experimental flavour physics it is necessary to correctly identify the final state particles. The two Ring-Imaging CHerenkov detectors (RICH1 and RICH2) are the first part of the particle identification (PID) process. They are used to identify charged hadrons like pions, kaons and protons by measuring their Cherenkov radiation. When a charged particle passes through a radiator with refractive index n and its velocity exceeds the velocity of light c/n inside the radiator, photons are emitted on a cone around the particle. The opening angle θ_c

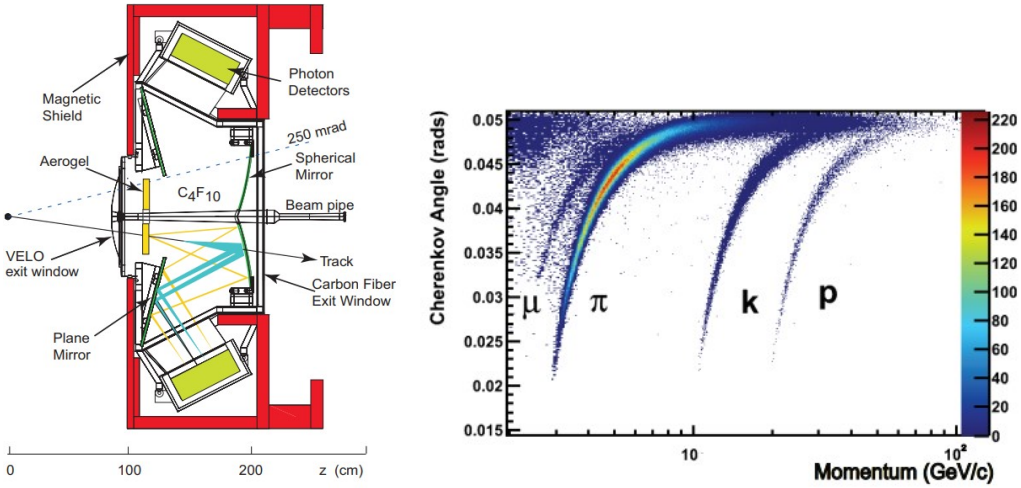

Figure 3.4: Layout of the RICH1 detector (left) and Cherenkov angle versus momentum for C_4F_{10} (right). The aerogel was removed for Run 2. [18, 21]

is given by the velocity v of the particle and the refractive index n :

$$cos(\theta_c) = \frac{c}{vn}. \tag{3.1}$$

In figure 3.4, the relation between the Cherenkov angle and the momentum of the particle is shown and it is clearly visible that the different kinds of particles lie in different bands.

RICH1 is situated between the VELO and the TT and uses C_4F_{10} gas as radiator covering the lower momentum range from 2 to 60 GeV/c. It covers the whole acceptance of the detector. RICH2 is placed after T3 and uses CF_4 gas to cover momenta from 50 to 100 GeV/c. It has only a limited horizontal (vertical) angular acceptance from 15 to 120(100) mrad. In both detectors, spherical and flat mirrors are used to focus the Cherenkov light and reflect it out of the acceptance where it is read out by photon detectors. Figure 3.4 shows the layout of RICH1.

3.2.5 Calorimeters

The calorimeter system is comprised of four sub-detectors. It is used to identify electrons, photons and hadrons and measure their energies and positions. The first detector is the Scintillating Pad Detector (SPD). As only charged particles are detected by the SPD, it is used to distinguish photons from electrons, which both deposit energy in the form of electromagnetic showers in the PreShower detector (PS) that follows behind the SPD. The two detectors are separated by a lead sheet that initiates the showers. The energy and position of photons and electrons is then measured by the Electromagnetic CALorimeter (ECAL). It consists of alternating

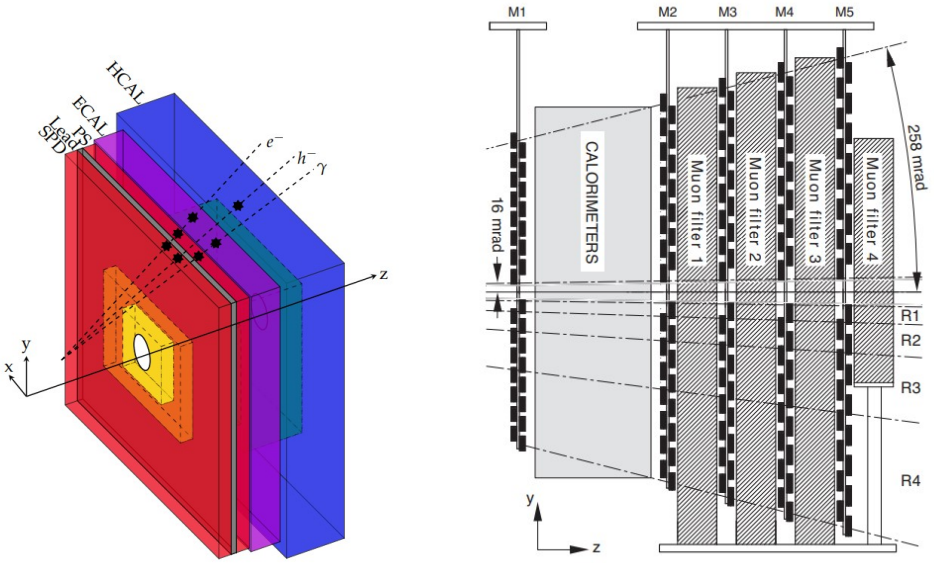

Figure 3.5: Layout of the calorimeter system (left) and the muon system (right) [22, 18]

layers of lead and scintillator tiles. The Hadronic CALorimeter (HCAL), which is the last of the four sub-detectors of the system, is built similarly to the ECAL and measures energy and position of hadrons. It uses iron instead of lead as absorber material. The absorber material is used to induce electromagnetic or hadronic showers, respectively. The particles produced in the showers are converted to photons in the scintillator, which are read out by photomultiplier tubes. The energy of the primary particle can then be measured as it is proportional to the number of photons. Figure 3.5 shows the arrangement of the calorimeter system.

3.2.6 Muon System

The muon system consists of five muon stations, M1-M5, and is located at the end of the detector. It measures momentum and transverse momentum of muons. The stations M2-M5 are behind the calorimeters and separated by 80 cm thick iron absorbers. This guarantees that only muons can travel through the whole detector and reach the last station. The station M1 is placed in front of the calorimeters (see figure 3.5), which improves the transverse momentum measurement for the trigger system that is explained in section 3.4. The stations are mainly built from Multi Wire Proportional Chambers (MWPC). The muons ionize the gas within the chambers proportional to their energy and the charges created by this ionization process reach the read out electronics due to an electric field generated by electrodes.

3.3 Particle Identification

Particle identification algorithms combine the information from the sub-detectors to discriminate between different particle types in two ways [23]. The first method calculates a so-called log-likelihood difference (DLL). For each track, a likelihood $\mathcal{L}$ for different particle mass hypotheses is computed. Since pions are the most abundant particles in the detector, they are chosen as a reference. The likelihoods of each sub-detector are added linearly. The log-likelihood difference relative to the pion hypothesis is then given by:

$$\mathrm{DLL}_X = \Delta \log \mathcal{L}_{comb}(X - \pi) = \log \mathcal{L}_{comb}(X) - \log \mathcal{L}_{comb}(\pi), \tag{3.2}$$

where X is the electron, muon, kaon or proton mass hypothesis. The respective combined likelihoods for a particle hypothesis are given by $\mathcal{L}_{comb}(X)$ and $\mathcal{L}_{comb}(\pi)$. A second method was developed to additionally take into account correlations between the information from different sub-detectors. Based on multivariate analysis techniques, a neural network was trained to discriminate the particle species. It combines information from all sub-detectors into one output variable for each particle hypothesis X. The variables are referred to as ProbNN_X and range between 0 and 1.

3.4 The LHCb Trigger System

The LHC provides pp collisions with a rate of 40 MHz. For the LHCb detector, it is not possible to read out all sub-detectors and store their data at this rate. Furthermore, not all events are of interest, since only a fraction of them contain particles with c- and b-quarks. To reduce the event rate and select the events of interest, a trigger system is employed. It consists of three consecutive stages. The first stage, also called L0, is a hardware based trigger that uses information from the calorimeters and muon system, as they are the only sub-detectors that can be read out at the full 40 MHz. It selects particle candidates according to their transverse energy and transverse momentum. The thresholds for this cut are individual for each sub-detector. This reduces the rate to 1 MHz and the remaining events are passed on to the first software based high-level trigger stage, HLT1. It uses information from the VELO and the tracking stations to partially reconstruct events by searching for primary vertices and tracks. So called trigger lines apply simple cuts on transverse momenta and impact parameters. For some trigger lines these cuts are optimised based on multivariate analysis (MVA) techniques. This reduces the rate down to 150 kHz and the data is written to a buffer before being passed on to the second high-level trigger stage, HLT2. The intermediate storage on a buffer allows for detector calibrations and alignments in between the two trigger stages. In HLT2, a full event reconstruction using information of all sub-detectors is possible. The trigger lines for this stage can be divided into two main categories. Inclusive lines select

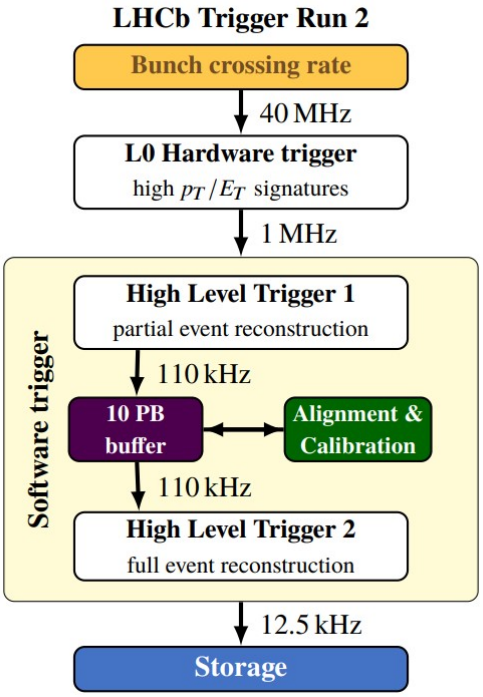

Figure 3.6: The LHCb trigger system. Events have to pass through three consecutive trigger stages before they are saved. In between the two high-level triggers, a buffer allows for detector alignments and calibrations.[25]

for general topological conditions of decays whereas exclusive lines are specifically designed for a certain final state. After all three trigger stages, the output rate is reduced to 12.5 kHz and the data is written to disk (see figure 3.6). There are two strategies to store the data. The first one is to store the complete detector output which allows an offline reconstruction afterwards. This uses a large amount of storage space per event. The second strategy is the so called turbo stream, where only information of the reconstructed objects is saved and all other data is discarded. In Run 2, both strategies were applied depending on the specific decay.
In the event reconstruction, information about which part of the event was responsible for a certain trigger decision is accessible. By investigating the signal candidate and the rest of the event independently, the events can be put into several trigger categories [24]. The relevant trigger categories in this thesis are:

- Triggered On Signal (TOS): The signal candidate itself is sufficient to produce a positive trigger decision.
- Triggered Independent of Signal (TIS): When removing the signal candidate from the event, the rest of the event is sufficient to produce a positive trigger decision.

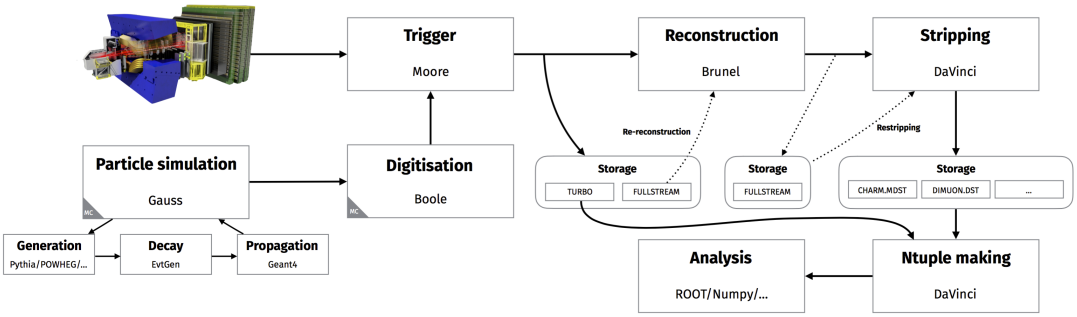

Figure 3.7: The LHCb data flow for Run 2. [35]

3.5 Simulation and Data Flow

In addition to real proton-proton collision data, this analysis also makes use of simulated data. Simulated events, also called Monte Carlo (MC) events, have to match data as close as possible. This is why they are processed similarly to real data. The LHCb MC event simulation is done in several steps . The framework GAUSS [26] controls the generation of events and the interactions of particles with the detector. First, the event generator PYTHIA [27] simulates the proton-proton collision. The decays of the resulting particles is simulated by EvtGen [28]. Afterwards, Geant4 [29] is used to simulate how particles propagate through and interact with the detector. Before this step, generator level cuts can be applied. In the next step, the BOOLE application [30] simulates the response of the different sub-detectors to mimic the detector output for real data. This includes the response of the hardware trigger L0. After this, all following processes are the same for simulated and real data. The software application MOORE [31] handles the high level trigger stages HLT1 and HLT2 described above. For the full stream, the data and simulated data is passed onto the BRUNEL application [32] for the offline reconstruction of the events. In a filtering process called stripping, further cuts are applied to the reconstructed data by decay specific stripping lines. These stripping lines are similar to the trigger lines used in the trigger process. The stripping is done by the DAVINCI application [33] and the output is stored in files accessible by software packages like ROOT [34] for analysis. In the turbo stream, the output of MOORE is directly passed onto the DAVINCI application that produces the files used in analysis. The full data flow of the LHCb experiment is shown in figure 3.7.

4 Analysis Strategy and Tools

This chapter describes the strategy used to analyse the data collected by the LHCb experiment. Furthermore, the analysis tools used in this thesis are presented. The data samples are available as so called ROOT files and are selected, fitted and evaluated within the ROOT framework [34]. The output of two types of multivariate classifiers, neural networks [36] and boosted decision trees [37], is used in the event selection. For the correction of trigger efficiencies, the TISTOS method [24, 38] is used.

4.1 Strategy

The goal of this analysis is to perform a branching fraction measurement of the decay $D^0 \to K^-\pi^+e^-e^+$. In principle, the absolute branching fraction of a decay mode of the D^0 meson can be measured by determining the total yield of D^0 mesons produced during data taking, and the number of events, where the D^0 meson decayed into the studied mode. However, this requires a precise knowledge of the D^0 meson production rate which is not known. Another approach is to measure the branching fraction relative to a normalization channel. Typically, a well measured decay with similar topology is used. For this analysis, the decay $D^0 \to K^-\pi^+\pi^-\pi^+$ is chosen as it has in addition to the K^- and π^+ two more tracks. In the following, the decays $D^0 \to K^-\pi^+e^-e^+$ and $D^0 \to K^-\pi^+\pi^-\pi^+$ are referred to as signal channel and normalization channel, respectively. The ratio between the branching fractions for signal and normalization channel is given by:

$$\frac{\mathcal{B}_{D^0\to K^-\pi^+e^-e^+}}{\mathcal{B}_{D^0\to K^-\pi^+\pi^-\pi^+}} = \frac{N_{D^0\to K^-\pi^+e^-e^+}}{N_{D^0\to K^-\pi^+\pi^-\pi^+}} \cdot \frac{\epsilon_{D^0\to K^-\pi^+\pi^-\pi^+}}{\epsilon_{D^0\to K^-\pi^+e^-e^+}}, \tag{4.1}$$

where $N_{D^0\to K^-\pi^+e^-e^+}$ and $N_{D^0\to K^-\pi^+\pi^-\pi^+}$ denote the observed event yields and $\epsilon_{D^0\to K^-\pi^+e^-e^+}$ and $\epsilon_{D^0\to K^-\pi^+\pi^-\pi^+}$ are the total reconstruction and selection efficiencies, respectively for signal and normalization channel. Multiplying with the branching fraction of the normalization channel results in a formula for the signal decay branching fraction:

$$\mathcal{B}_{D^0\to K^-\pi^+e^-e^+} = \frac{N_{D^0\to K^-\pi^+e^-e^+}}{N_{D^0\to K^-\pi^+\pi^-\pi^+}} \cdot \frac{\epsilon_{D^0\to K^-\pi^+\pi^-\pi^+}}{\epsilon_{D^0\to K^-\pi^+e^-e^+}} \cdot \mathcal{B}_{D^0\to K^-\pi^+\pi^-\pi^+}. \tag{4.2}$$

Thus, determining the ratios of the yields and efficiencies is sufficient for the measurement. Furthermore, the similar nature of both decay channels lead to cancellations of systematic effects in the efficiency ratio, introduced, for example, by

the decay topology. The only external input of the measurement is the branching fraction of the normalization channel. This has already been measured [39, 40, 41] with a 1.7% precision:

$$\mathcal{B}_{D^0\to K^-\pi^+\pi^-\pi^+} = (8.22 \pm 0.14) \times 10^{-2}[42]. \tag{4.3}$$

To determine the event yields $N_{D^0\to K^-\pi^+e^-e^+}$ and $N_{D^0\to K^-\pi^+\pi^-\pi^+}$, a selection is needed to filter out respective decay candidates from the recorded proton-proton collision data. The relevant data samples are obtained by stripping lines that filter the possible candidates (see chapter 5). At this point, the samples contain candidates, where at least one trigger line for each trigger stage has fired. This includes also candidates, where the event was triggered independent of the signal candidate by trigger lines for other particles or decays. To simplify the evaluation of the trigger efficiency, trigger requirements for each of the different trigger stages are explicitly applied. The trigger requirements are defined to keep as many signal events as possible with lines selecting expected event characteristics of the decays. Afterwards, a cut based selection is applied to further reduce the amount of background candidates. Apart from stronger requirements on kinematic variables and their reconstruction qualities, cuts are applied on particle identification variables of the final state particles. The selection of the normalization channel is kept as similar as possible to the selection of the signal events to benefit from possible cancellations in the efficiency ratio. After the selection, the mass distributions of the D^0 meson is fitted to obtain the number of candidates, $N_{D^0\to K^-\pi^+e^-e^+}$ and $N_{D^0\to K^-\pi^+\pi^-\pi^+}$.

In a second step, the efficiency ratio is determined. The reconstruction and selection efficiencies are estimated using simulated samples of signal and normalization channel. Differences between data and simulation are taken into account by data-driven corrections. This is done using calibration data from other decays.

Finally, the yields and efficiencies of signal and normalization channel are inserted into equation 4.2 to obtain the branching fraction of $D^0 \to K^-\pi^+e^-e^+$.

4.2 ROOT

The object-oriented analysis framework ROOT was designed in the 1990's for data analysis high-energy physics. The first version was released in 1995. ROOT is based on the C++ programming language and is designed to manage, analyze and manipulate very large data sets. The organization of data is based on a tree like structure with subdivisions like branches and leaves. ROOT has many features to access and visualize data in multi dimensional histograms. Furthermore, it provides a number of different tools to combine, fit and analyse large data sets.

4.3 Multivariate Methods

Multivariate analysis techniques can be used to classify data samples into different categories of interest. The general assumption for a classification problem is that there exists a function f mapping a set of input variables $\mathbf{x}$ from the dataset to the corresponding class label y: $f(\mathbf{x}) = y$. The goal of a multivariate method is to find an optimal approximation $\hat{f}$ of f. By using a labeled training sample consisting of variable-label pairs $(\mathbf{x}, y)$, an algorithm can be trained to find $\hat{f}$. This is done by minimizing a so-called loss function $L(y, \hat{f}(\mathbf{x}))$ that determines the quality of the label prediction [37]. The following sections describe how neural networks and boosted decision trees classify data samples.

4.3.1 Neural Networks

The fundamental building block of a neural network is a neuron. It is a simplified model of a biological neuron that takes a set of input variables to combine them to produce an output value. In a neural network, many such neurons are connected in a layered structure, where the output of one layer is the input of the next layer. The first layer in the neural network is the input layer and the last layer is the output layer. The layers in between are often called *hidden layers*. The basic structure of a neural network is shown in figure 4.1a. The output function a for a single neuron can be described by a linear transformation of the input vector $\mathbf{x}$, followed by a non-linear activation function g:

$$a(\mathbf{x}) = g(\mathbf{w}\mathbf{x} + b), \tag{4.4}$$

where $\mathbf{w}$ is a set of neuron specific weights and b describes the neuron specific bias (see figure 4.1b). The initial weights and biases are random. During the training process, they are optimized by minimizing the loss function [36].

The PID variables ProbNN are based on six one-layer neural networks corresponding to the particle types electron, muon, pion, kaon, proton and ghost. A so called ghost particle corresponds to a reconstructed track that does not belong to a real particle. Each network is trained to separate its particle type from the others [43].

4.3.2 Boosted Decision Trees

Another method for solving a classification problem is to use decision trees [36]. A decision tree is particularly suitable for binary decisions, for example to separate a dataset into signal and background events. Using a labeled training sample, a tree is built by successively adding decision nodes. Starting from the root node, which contains the whole training sample, the data is split into two subsets or branches according to a binary decision on an input variable. The variable with the highest signal to background separation is chosen. In the next step, the resulting branches

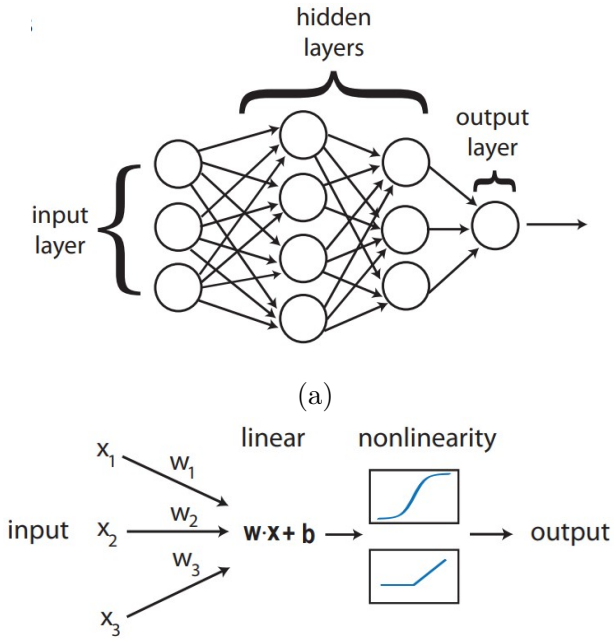

Figure 4.1: Architecture of a neural network [36]. (a): Many neurons are connected in a layered structure. The output of one layer is the input for the next layer. (b): The output function of a single neuron is a linear combination of the input vector, followed by a non-linear activation function.

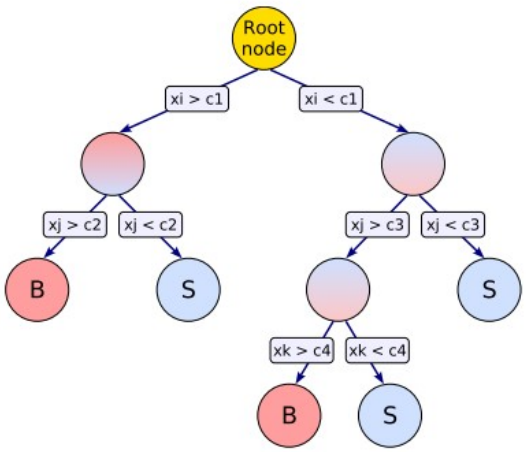

Figure 4.2: Example of a decision tree [44]. At each node, one of the variables $\mathbf{x}$ is used to split the sample in two branches. Signal and background leaves are marked with S and B, respectively.

are split in the same way. This procedure is repeated until the whole tree is built. The endpoints or *leaves* of the tree are then labeled as either signal or background depending on which type of event dominates. Afterwards, the resulting decision tree can be used to classify unlabeled candidates by propagating them through the tree structure. Figure 4.2 shows a diagram of a decision tree.

In principle, new nodes can be attached to the tree until all leaves contain only signal or background training events. However, this leads in general to so-called over-fitting, where the decision tree is modeling the statistical fluctuations of the training sample. To reduce over-fitting and to control the complexity, the depth of a decision tree is usually limited, which restricts the prediction power of the tree. In addition, single decision trees are sensitive to details of the training sample and are thus referred to as *weak learners*. In a process called *boosting*, several weak learners can be combined to form a significantly improved classifier [37]. A boosted decision tree is constructed by an iterative procedure. First, a shallow decision tree is built on the original, unweighted training sample. Each event that is wrongly classified by this tree receives an increased weight. With the re-weighted training sample, the next decision tree is built. This procedure is repeated to produce a series of N decision trees. Each new tree improves on the errors of previous trees. The final output of the boosted decision tree is a weighted sum of the whole series:

$$\hat{f}(\mathbf{x}) = \sum_{k=1}^{N} \alpha_k T_k(\mathbf{x}), \tag{4.5}$$

where T_k is the tree of the k-th iteration and α_k is the corresponding weight. To classify a candidate, each tree assigns a score depending on the prediction. For

example, if the candidate reaches a signal leaf, its score is +1 and if it reaches a background leaf, the candidate gets a score of −1. For the final prediction, the scores are summed according to equation 4.5. A high resulting value corresponds to a high probability for the candidate to be signal. If the value is low, it is probably background.

In the selection (see chapter 5), the output of a boosted decision tree is used in the HLT2 line for the normalization channel to select signal candidates.

4.4 TISTOS Method

For the branching fraction measurement, the efficiency of the trigger selection has to be determined. One way to calculate the efficiency of a trigger is to determine the fraction of signal events within the acceptance of the detector, accepted by the trigger decision:

$$\epsilon_{Trig} = \frac{N_{Trig|Acc}}{N_{Acc}}, \tag{4.6}$$

The fundamental problem with this method is that the number of signal events in the acceptance, N_{Acc}, is not known for data. The trigger efficiency for data could therefore be estimated using simulated samples. However, possible differences between simulation and data are not known in this approach. An alternative solution is to determine the efficiency on a sub-sample of the data with the so-called TISTOS method [24]. To guarantee that the trigger efficiency of the sub-sample corresponds to the true efficiency, the sub-sample has to be triggered in an independent way. This is done by choosing events passing a trigger requirement that is independent from the evaluated trigger decision. For this, the trigger categories introduced in chapter 3.4 are used. For a given TOS trigger decision, the efficiency is calculated using a data sample with high purity. First, a TIS trigger requirement, that is independent of the investigated TOS trigger, is defined. The efficiency of the TOS trigger is then given by [38]:

$$\epsilon_{TOS} = \frac{N_{TIS\&TOS}}{N_{TIS}}, \tag{4.7}$$

where N_{TIS} is the number of events satisfying the TIS requirement and $N_{TIS\&TOS}$ is the number of events among them, that passed in addition the TOS decision.

5 Event Selection

This chapter describes the event selection used to reduce the amount of background events in the data samples. Apart from the data samples for signal and normalization channel, simulated samples corresponding to signal and peaking background components of the two channels are used. Only for the signal channel, a peaking background component, coming from wrongly reconstructed $D^0 \to K^-\pi^+\pi^-\pi^+$ decays, is expected (see below). The samples are required to pass respective stripping lines and trigger requirements. Afterwords, additional kinematic, topological and vertex quality cuts are imposed as well as requirements on the PID variables.

5.1 Event Samples

This analysis uses proton-proton collision data collected by the LHCb detector in 2017 and 2018 during Run 2, corresponding to an integrated luminosity of $3.8\,\mathrm{fb}^{-1}$.

After the event candidates have passed all three stages of the trigger system described in chapter 3.4, they are further filtered by the stripping. The candidates used for the signal decay $D^0 \to K^-\pi^+e^-e^+$ are selected by the stripping line *DstarPromptWithD02HHLLLine* and the normalisation candidates are selected by its control line *DstarPromptWithD02HHMuMuControlLine* (see below). Both stripping lines apply the same selection on the candidates apart from PID requirements. Additionally, the control stripping line introduces a prescale of 0.5 to the normalization sample reducing computing resources by removing half of all event candidates. A detailed list with the stripping line requirements is shown in table 5.1.

The reconstruction of event candidates, used to apply the stripping lines, is done in a bottom-up approach: First, four final state particles are combined to reconstruct the D^0 meson. Afterwards, a pion is matched to the D^0 meson candidate to form a $D^{*\pm}$ meson. All four daughter particles of the D^0 are required to have a minimal momentum p and transverse momentum p_T and a good track quality is required by a cut on the ratio of the χ^2 and the number of degrees of freedom, dof, of the track fits. In addition, it is required that all tracks are displaced with respect to the primary vertex to guarantee that the decay vertex of the D^0 meson is separated from the primary vertex as the D^0 meson is expected to fly a short distance within the detector. This is ensured by a cut on the significance of their impact parameters, IP χ^2. The reconstruction of the D^0 meson decay is performed only for kaons and electrons which pass their respective PID requirement. The reconstructed mass of the D^0 meson is required to be in a mass window around the

known mass according to the Particle Data Group (PDG). This mass cut is applied first to the reconstructed mass resulting from just combining the four-vectors of the decay daughters and afterwards also when reconstructing the D^0 meson with additional constraints, for example fixing one single decay vertex. These two cuts can be found in table 5.1 under $m(hh\ell\ell)$ and $m(D^0)$, respectively. Furthermore, there is a maximal value for the distance of closest approach (DOCA) for all track combinations of the D^0 daughters and for at least one of them, the significance of the impact parameter has to be even higher than the previously defined cut value. This increases the probability that the particles originate from one common decay vertex. For the D^0 meson, there are cuts on the quality of the vertex, the significance of the flight distance, FD χ^2, and the significance of the impact parameter. In addition, there is a minimum requirement on the momentum p and transverse momentum p_T. This further reduces possible background candidates. The direction angle (DIRA) is defined as the cosine of the angle between the direction of the combined momentum of the decay daughters and the vector from primary to secondary vertex. Requiring that the DIRA of the D^0 meson is almost one ensures that both directions are aligned. The pion coming from the prompt decay of a $D^{*\pm}$ meson has to fulfill a minimum requirement on the transverse momentum p_T and its track has to be of good quality. Furthermore, the difference between the masses of the $D^{*\pm}$ meson and D^0 meson, Δm, is restricted to lie in a window around the mass of the pion. Similar to the cut for the D^0 mass, this cut is also applied before and after the full $D^{*\pm}$ reconstruction. The D^0 meson and the slow pion have to come from the same vertex, which is ensured by a cut on DOCA. In addition to that, there is a minimum requirement on the transverse momentum of the particle pair. Lastly, the quality of the $D^{*\pm}$ vertex is guaranteed with a cut on χ^2/dof of the vertex fit.

The stripping line for the normalization candidates is almost identical to the one for the signal candidates (see table 5.1). The PID requirement is only applied to the kaon since we select final states with pions and one kaon. Additionally, the data sample is prescaled by a factor of 0.5. This has to be taken into account in the branching fraction calculation.

5.2 Simulated Data

In addition to the recorded collision data, simulated samples of the signal and normalization decay channel are generated using LHCb simulation software. This is done for each year separately to account for different Run conditions. The simulated samples are used in order to estimate reconstruction and selection efficiencies and to determine the shapes of the models used to fit to mass distributions. Here the idea is to find a way to separate signal and background in the data samples. The exact fitting procedure is described in chapter 6.

Particle	Variable		Signal mode $D^0 \to K^-\pi^+e^-e^+$ 2017-2018 (S29r2,S34)	Normalization mode $D^0 \to K^-\pi^+\pi^-\pi^+$ 2017-2018
K, π, e	p	$>$	$3\,\mathrm{GeV}/c$	$3\,\mathrm{GeV}/c$
	p_T	$>$	$300\,\mathrm{MeV}/c$	$300\,\mathrm{MeV}/c$
	Track χ^2/dof	$<$	3	3
	IP χ^2	$>$	3	3
e	DLL_e	$>$	-2	
K	DLL_K	$>$	-5	-5
$(hh\ell\ell)$	m$(hh\ell\ell)$	$>$	$m_{\mathrm{PDG}} - 240\,\mathrm{MeV}/c^2$	$m_{\mathrm{PDG}} - 240\,\mathrm{MeV}/c^2$
		$<$	$m_{\mathrm{PDG}} + 240\,\mathrm{MeV}/c^2$	$m_{\mathrm{PDG}} + 240\,\mathrm{MeV}/c^2$
	max DOCA	$<$	$0.3\,\mathrm{mm}$	$0.3\,\mathrm{mm}$
	max IP χ^2	$>$	9	9
D^0	m(D^0)	$>$	$m_{\mathrm{PDG}} - 220\,\mathrm{MeV}/c^2$	$m_{\mathrm{PDG}} - 220\,\mathrm{MeV}/c^2$
		$<$	$m_{\mathrm{PDG}} + 220\,\mathrm{MeV}/c^2$	$m_{\mathrm{PDG}} + 220\,\mathrm{MeV}/c^2$
	Vertex χ^2/dof	$<$	20	20
	FD χ^2	$>$	16	16
	DIRA	$>$	0.9999	0.9999
	IP χ^2	$<$	36	36
	p_T	$>$	$2\,\mathrm{GeV}/c$	$2\,\mathrm{GeV}/c$
	p	$>$	$3\,\mathrm{GeV}/c$	$3\,\mathrm{GeV}/c$
π_s	p_T	$>$	$120\,\mathrm{MeV}/c$	$120\,\mathrm{MeV}/c$
	Track χ^2/dof	$<$	3	3
$D^0\pi_s^+$	Δm	$>$	$125.4\,\mathrm{MeV}/c^2$	$125.4\,\mathrm{MeV}/c^2$
		$<$	$185.4\,\mathrm{MeV}/c^2$	$185.4\,\mathrm{MeV}/c^2$
	p_T	$>$	$2\,\mathrm{GeV}/c$	$2\,\mathrm{GeV}/c$
	max DOCA	$<$	$0.3\,\mathrm{mm}$	$0.3\,\mathrm{mm}$
$D^{*\pm}$	Δm	$>$	$129.4\,\mathrm{MeV}/c^2$	$129.4\,\mathrm{MeV}/c^2$
		$<$	$181.4\,\mathrm{MeV}/c^2$	$181.4\,\mathrm{MeV}/c^2$
	Vertex χ^2/dof	$<$	20	20

Table 5.1: Stripping selection requirements.

This analysis uses three simulated data samples. In addition to the two samples for the signal decay $D^0 \to K^-\pi^+e^-e^+$ and the normalisation decay $D^0 \to K^-\pi^+\pi^-\pi^+$, where the particles are reconstructed with the same identities as they were produced by the decay simulation, there is also a sample needed for $D^0 \to K^-\pi^+\pi^-\pi^+$ decays for which a $\pi^+\pi^-$-pair is wrongly reconstructed as a pair of electrons resulting in an event associated to the signal decay. Further physical background components are not expected to contribute.

In order to be able to estimate the efficiencies, the simulated data is processed in exactly the same way as the proton-proton collision data all the way from the reconstruction process to the last cut of the selection.

5.3 Trigger Requirements

After the data has passed through the stripping process, the first step of the offline selection is to explicitly apply trigger criteria for the three trigger stages. This simplifies the evaluation of trigger efficiencies while keeping as much signal events as possible. For all stages, triggers in the TOS category (see chapter 3.4) are used. The trigger efficiencies are evaluated from the simulated samples. Thus, by using TOS decisions, only the simulation of the signal part of the event takes influence on the accuracy of the resulting trigger efficiencies.

At the L0 hardware-stage, one of the D^0 daughter particles is required to have triggered the respective hadron or electron TOS decision. Therefore, the particle was detected by the corresponding sub-detector and the roughly estimated transverse momentum p_T of the particle was above a certain threshold. In addition to that, the number of hits in the SPD detector has to be below a certain maximum. This "global event cut" is applied to remove events that would take too long to process in the next stages. For the first stage of the software triggers, events have to satisfy the requirements of the HLT1TrackMVA or HLT1TwoTrackMVA trigger line. These lines use multivariate analysis techniques to decide if there was a track or two tracks, respectively, originating from a, to the primary vertex displaced, decay vertex.

At HLT2, signal events are required to pass the dedicated trigger line, called *Hlt2RareCharmD02KPieeDecision*. The cuts on the reconstructed events are shown in table 5.2.

As the cuts of the HLT2 line are similar to the cuts of the stripping line, only additional cuts will be explained in the following. However, some of the cuts are different in the HLT2 line. In HLT2, the event candidates are reconstructed differently to the offline reconstruction. The first step is to create a lepton and a hadron pair. These pairs are matched together to form a D^0 candidate. As before, a pion is then added to the D^0 meson to form a $D^{*\pm}$ candidate. There are a number of cuts on the properties of the lepton-pair. First, there is an upper limit on the invariant mass of the two leptons. They are required to carry transverse momentum and the DOCA of their tracks is small. When combining the two electrons into one object, the corrected mass for this is also limited to be below a maximum value. The flight distance of the dilepton object is required to be significant. Additional cuts on the transverse momentum of the four D^0 daughters and their sum, and a new requirement for the minimal DOCA of the particle track combinations is added. Furthermore, for the D^0 meson daughters, a cut is applied on the sum of the square roots of the significances of the impact parameters.

For the normalisation channel, there is no dedicated HLT2 trigger line available, since for this decay the turbo stream was used. As the turbo stream dataflow is

Particle	Variable		2017-2018
K, π, e	p	$>$	$3\,\mathrm{GeV}/c$
	p_T	$>$	$300\,\mathrm{MeV}/c$
	Track χ^2/dof	$<$	4
K, π	IP χ^2	$>$	2
e	IP χ^2	$>$	3
$(\ell\ell)$	m$(\ell\ell)$	$<$	$2100\,\mathrm{MeV}/c^2$
	Σp_T	$>$	$0.\,\mathrm{MeV}/c$
	DOCA	$<$	0.1 mm
Dilepton object	FD χ^2	$>$	20
	FD	$>$	0 mm
$(hh\ell\ell)$	m$(hh\ell\ell)$	$>$	$1550\,\mathrm{MeV}/c^2$
		$<$	$2200\,\mathrm{MeV}/c^2$
	max p_T	$>$	$0.\,\mathrm{MeV}/c$
	Σp_T	$>$	$3000\,\mathrm{MeV}/c$
	min DOCA	$<$	0.2 mm
	max DOCA	$<$	0.3 mm
	max IP χ^2	$>$	3
D^0	m(D^0)	$>$	$1700\,\mathrm{MeV}/c^2$
		$<$	$2050\,\mathrm{MeV}/c^2$
	Vertex χ^2/dof	$<$	15
	FD χ^2	$>$	49
	DIRA	$>$	0.9999
	IP χ^2	$<$	25
	$\Sigma\sqrt{IP\chi^2}$	$>$	8
π_s	p_T	$>$	$120\,\mathrm{MeV}/c$
	Track χ^2/dof	$<$	5
$(D^0\pi_s)$	Δm	$>$	$130\,\mathrm{MeV}/c^2 - m_\pi$
		$<$	$180\,\mathrm{MeV}/c^2 - m_\pi$
D^{*+}	Δm	$>$	$130\,\mathrm{MeV}/c^2 - m_\pi$
		$<$	$170\,\mathrm{MeV}/c^2 - m_\pi$
	Vertex χ^2/dof	$<$	25

Table 5.2: Hlt2RareCharmD02KPieeDecision Trigger requirements. This line is used to trigger $D^0 \to K^-\pi^+e^-e^+$ events.

significantly different to the full stream, it is not feasible to take the data sample for the normalization channel. This is why for this analysis the inclusive trigger line *Hlt2CharmHadInclDst2PiD02HHXBDTDecision* is used to receive the decay candidates for the $D^0 \to K^-\pi^+\pi^-\pi^+$ sample from the full stream. This line is adapted to select for $D^{*\pm} \to \pi^\pm(D^0 \to)hhX$ decays, where the D^0 meson decays into 2 hadrons and other particles. The requirements on this line are shown in table 5.3. On top of simple cuts, it uses a boosted decision tree (BDT) that was trained

on MC samples. The input variables for the BDT were the flight distances of the D^0 and the $D^{*\pm}$, the cosine of the angle θ of the slow pion, the sum of the transverse momenta of the two hadrons, the transverse momentum of the slow pion, χ^2 of the D^0 vertex fit and the DOCA of the $D^{*\pm}$ daughters. The events are selected according to the BDT output.

Particle	Variable		Value
D^0	m	$<$	$2100\,\mathrm{MeV}/c^2$
	FD χ^2	$>$	20
D^*	m	$<$	$2300\,\mathrm{MeV}/c^2$
	Δm	$<$	$350\,\mathrm{MeV}/c^2$
	BDT output	$>$	1.33

Table 5.3: Hlt2CharmHadInclDst2PiD02HHXBDTDecision Trigger requirements. This line is used to trigger $D^0 \to K^-\pi^+\pi^-\pi^+$ events.

5.4 Pre-selection

After the trigger lines are applied, the samples still contain a considerable amount of background events (see figure 5.2b). Both samples of signal and normalization channel contain background events, where random tracks are associated to the respective decays. This is called combinatorial background. Furthermore, the signal sample contains $D^0 \to K^-\pi^+\pi^-\pi^+$ events for which two pions are mis-identified as electrons. The reason for this is that the branching fraction for $D^0 \to K^-\pi^+\pi^-\pi^+$ decays is about four orders of magnitude higher compared to the expected branching fraction of the signal channel. Thus, although PID cuts are applied by the stripping line, a fraction of these events are not yet rejected from the signal sample.

The figures 5.2a and 5.2b show the D^0 mass distribution for the signal sample before and after the trigger cuts, respectively. For both distributions, a peak at $\approx 1820\,\mathrm{MeV}/c^2$ is visible. This is not due to signal decays, but stems from mis-identified $D^0 \to K^-\pi^+\pi^-\pi^+$ decays. The peak is shifted to a lower value compared to the actual D^0 mass, which is around $1864\,\mathrm{MeV}/c^2$. The shift is a consequence of a wrong mass hypothesis for the pions in the reconstruction of $D^0 \to K^-\pi^+\pi^-\pi^+$ events as $D^0 \to K^-\pi^+e^-e^+$ candidates. The actual signal peak at the D^0 mass is not visible at this stage. In the pre-selection, further cuts are applied to the samples to remove background events while keeping as many signal candidates as possible.

As discussed previously, a dominant contribution to $D^0 \to K^-\pi^+e^-e^+$ decays are decays with a resonantly produced electron pair. For this analysis, electron pairs in the kinematic range of the ρ^0 and ω resonances are used to measure a partial branching fraction. Therefore, the invariant mass of the electron pair is required to be within a range around the masses of these resonances. The same minimum and

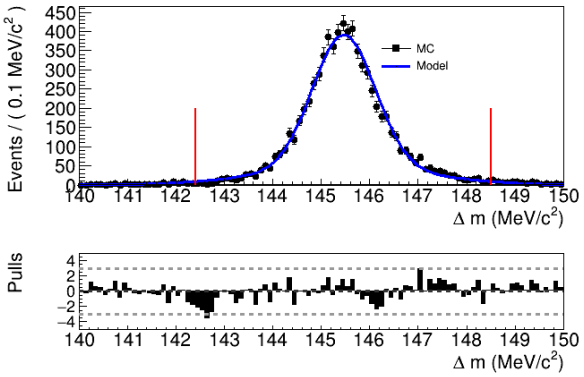

Parameter	Value
m_0	145.466 ± 0.009
σ_1	0.65 ± 0.02
σ_2	1.69 ± 0.06
N_1	5600 ± 200
N_2	1900 ± 200

Figure 5.1: Fit of the Δm distribution of the MC signal sample. Deviations between data and model are shown in a pull plot. The corresponding values for the parameters are given in the table on the right.

maximum values are chosen as in the BaBar measurement. This cut is applied to the signal sample before the pre-selection cuts.

First, the cut on the mass difference between the $D^{*\pm}$ and the D^0 is tightened. This removes a large fraction of combinatorial background, as it selects D^0 mesons originating from $D^{*\pm}$ decays. The cut range is defined by a fit to the Δm distribution of the MC signal sample. The fit function used to describe the shape of the Δm distribution is a double Gaussian. The fit results and parameter values can be found in figure 5.1. The cut window applied in the selection, indicated by two red lines, is set to the 3σ range around the mean drastically reducing the background contamination while keeping more than 99% of the signal.

The cuts on the transverse momentum, the significances of IP and FD, and the vertex quality of the D^0 are tighter. In addition, a cut on the p_T asymmetry within a cone around the transverse momentum of the $D^{*\pm}$ is imposed. In the decay tree fit, the whole decay chain is fitted including related constraints e.g. from decay vertices. If the fit does not converge, a negative value gets assigned to χ^2. Therefore, χ^2 of the decay tree fit is required to be greater than 0. Also, at least one primary vertex has to be identified. This further reduces the amount of background candidates.

In the reconstruction of particle tracks it can occur that hits are combined to form a track which does not correspond to the trajectory of a real particle. This results in ghost tracks. To counteract this effect, a multivariate classifier computes a probability for a track to be a ghost track. Only events, for which all final state particles have a ghost probability below 20%, are kept. Lastly, there are PID requirements imposed on the D^0 decay daughters. For this, the ProbNN variables are used. For the hadrons, the respective ProbNN value has to be above 60%.

Figure 5.2 shows the evolution of D^0 mass distribution of the selected signal events at different steps of the offline selection. In each plot, the reconstructed mass from the decay tree fit is shown. The cut on the D^0 mass in the stripping line is clearly visible in figure 5.2a. This cut is applied when the D^0 candidate is reconstructed using its daughter particles. Due to differences compared to the mass obtained by the decay tree fit, the cut edges are not sharp. The HLT2 line applies a tighter cut on the D^0 mass. Similarly, differences between the reconstruction in HLT2 and the decay tree fit lead to two shoulders/steps outside of the cut window. This effect can be neglected as the fits to the mass distribution are performed inside a smaller range compared to the HLT2 mass cut. The fitting procedure is discribed in chapter 6. The figures 5.2c and 5.2d show the D^0 mass distribution after the cut on the dilepton mass and after the cut on Δm, respectively. Applying the remaining cuts of the pre-selection results in the distribution shown in figure 5.2e. It is clearly visible that throughout the selection, the non-peaking combinatorial background component was significantly reduced. The regions to the right and left side of the peak contain less candidates in relation to the peak height compared to the data sample after the stripping. A large reduction is due to the cut on Δm. However, at this stage of the selection, the number of events with a misidentified pion pair is still dominating the signal sample, because the $D^0 \to K^-\pi^+\pi^-\pi^+$ decays have nearly the same topology. If these misidentified events are rejected, the actual signal peak, located at the D^0 mass, should become visible.

5.5 Electron PID Requirement and Bremsstrahlung Categories

The last step of the selection is to reduce the mis-identified background component of the signal channel sample. For this, a cut is applied to the ProbNN PID variable of the electrons.

However, there is an additional complication which needs to be taken into account. As explained in chapter 2, electrons can emit bremsstrahlung through interactions with matter. In these processes they lose energy. If bremsstrahlung is emitted after the magnet, the energy deposits of the electron and the emitted photon end up in the same region of the ECAL and their combined energy gets attributed to the electron. The energy measurement matches the initial energy of the electron. In the case in which the photon is emitted before the magnet, the flight direction of the electron still changes according to the magnetic field. The flight path of the photon, which does not carry electric charge, is not affected by the magnetic field. Thus, the two particles deposit their energy in different regions of the ECAL and the energy can not be recovered leading to a lower energy measurement for the electron. This is illustrated in figure 5.3: If bremsstrahlung is emitted before the magnet, there

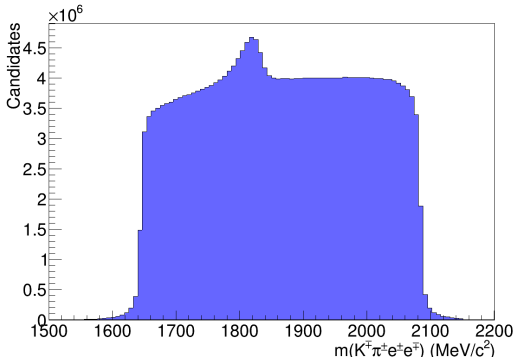

(a) Stripped data before the offline selection

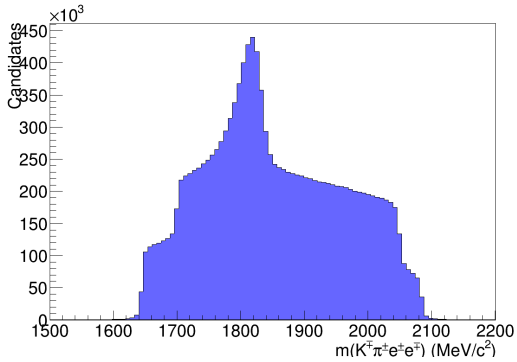

(b) After applying the trigger requirements

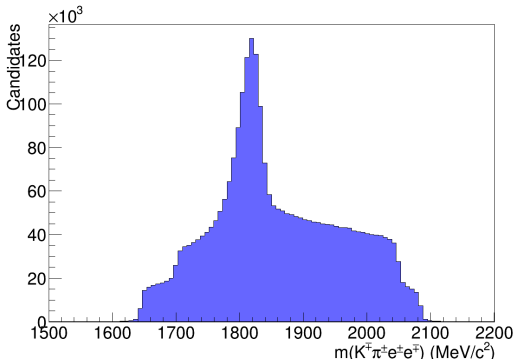

(c) After applying the dilepton mass cut

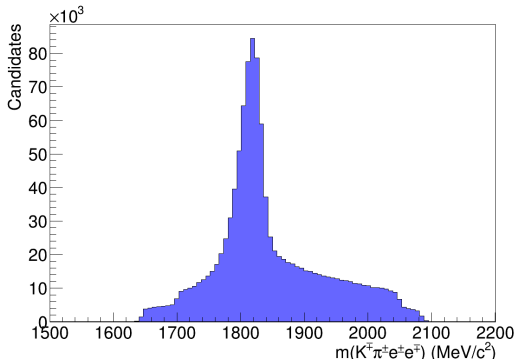

(d) After applying the cut on Δm

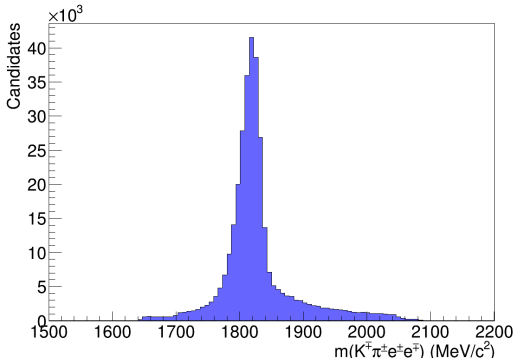

(e) After the pre-selection

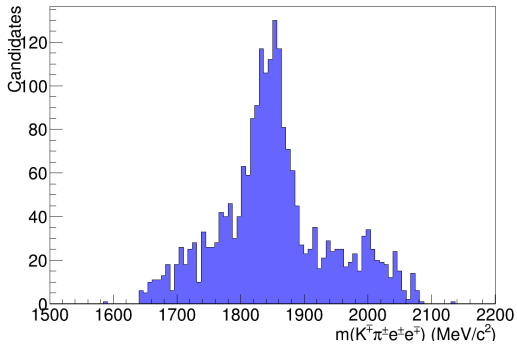

(f) After the PID cut on the electrons

Figure 5.2: Histograms of the D^0 meson mass distribution at different steps of the offline selection.

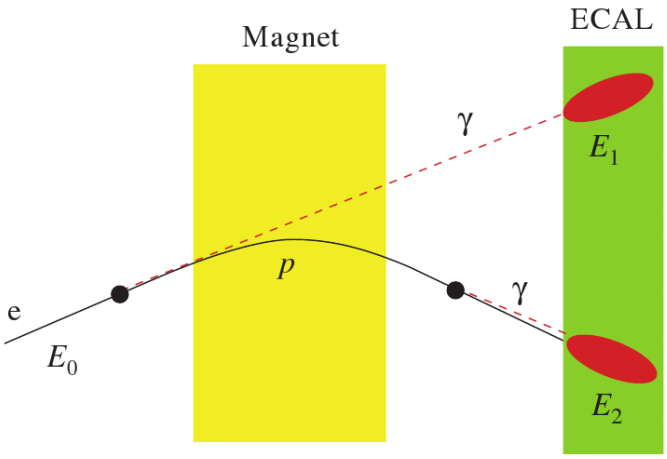

Figure 5.3: Illustration of an electron flying through the detector [45]. Two bremsstrahlung photons are emitted before and after the magnet, respectively.

are two destinct regions, E_1 and E_2, where the energy is deposited in the ECAL. This effect is accounted for by an algorithm in the electron reconstruction. It recovers bremsstrahlung by matching photons to electrons. The measured energy of the photon is added to the electron energy. However, this approach is not perfect as photons could be wrongly associated to electrons or bremsstrahlung could not be detected. For these cases, the measured energy of the electron is too high or still too low, respectively.

Whether or not bremsstrahlung photons are found and added by the algorithm has a significant influence on the electron reconstruction and thus also on the shape of the D^0 mass distribution. This is why the samples for the signal channel are divided into two bremsstrahlung categories: Decay candidates, where for neither of the two electrons additional bremsstrahlung was found are in the first category, referred to as **brem0**. The second category contains candidates, where for at least one of the electrons, one or more bremsstrahlung photons were found and added. This category is referred to as **brem1+**.

With higher cuts on the ProbNN value of the electrons, the mis-identified background is further suppressed. However, if the cut value is chosen too high, a large fraction of $D^0 \to K^-\pi^+e^-e^+$ candidates is lost. Therefore, this cut has to be optimised by determining signal and background yields for different cut values in both bremsstrahlung categories. The optimization of the electron PID requirement was done in a bachelor thesis previous to this work [46]. A figure of merit (FOM) was used to determine an optimal cut value. It is defined by:

$$FOM = \frac{N_{Sig}}{\sqrt{N_{Sig} + N_{Bkg}}}, \tag{5.1}$$

where N_{Sig} and N_{Bkg} are the signal and background yields. They are obtained by a fit to the D^0 mass distribution, equivalent to the fit described in chapter 6.1. The FOM was significantly improved by the PID cut in the **brem0** category. The optimal cut value for this sample was found to be:

$$ProbNN_E > 0.6. \tag{5.2}$$

For the **brem1+** category, a high FOM is found for all tested cut values. For simplicity, to use the MC event ratio between the two categories for the misidentified background component, the cut value of 0.6 was chosen for both categories.

The resulting D^0 mass distribution after this cut is shown in 5.2f. In comparison to figure 5.2e, the peak is shifted to a higher mass close to the PDG mass of the D^0 meson. Therefore, the misidentified background component was sufficiently reduced for the signal component to be visible. All pre-selection and PID requirements are listed in table 5.4.

Particle	Variable		Signal mode	Normalization
Dilepton object	m($\ell\ell$)	$>$	675 MeV/c^2	
		$<$	875 MeV/c^2	
K, π, e	Track ghost probability	$<$	20%	20%
K	ProbNN$_K$	$>$	60%	60%
π	ProbNN$_\pi$	$>$	60%	60%
e	ProbNN$_e$	$>$	60%	
D^0	p_T	$>$	2.5 GeV/c	2.5 GeV/c
	IP χ^2	$<$	10	10
	FD χ^2	$>$	36	36
	Vertex χ^2/dof	$<$	10	10
D^{*+}	Δm	$>$	142.4 MeV/c^2	142.4 MeV/c^2
		$<$	148.5 MeV/c^2	148.5 MeV/c^2
	Cone p_T asymmetry	$>$	-0.4	-0.4
	Decay tree fit χ^2	$>$	0	0
π_s	Track ghost probability	$<$	20%	20%
	Number of primary vertices	$>$	0	0

Table 5.4: Pre-selection and PID requirements.

6 Mass Fits

The event yields needed for the branching fraction calculation are determined by fits to the reconstructed D^0 invariant mass distribution. First, signal and peaking background shapes are determined using the simulated samples. Then, the individual signal and background components are combined in models that are fitted to the data samples. The resulting yields for signal and normalization channel are used in the branching fraction calculation.

6.1 Signal Channel

After the selection process, the data sample for the signal channel is comprised of the following three components:

- signal $D^0 \to K^-\pi^+e^-e^+$ events
- misidentified $D^0 \to K^-\pi^+\pi^-\pi^+$ events
- combinatorial background.

Further background components are excluded as the selection puts strong requirements on the event topology. Physical backgrounds from other misidentified D^0 decays are not visible, the expected observed branching fraction for these decays is below the statistical sensitivity in the data sample. Single events from these decays are expected to be covered by the combinatorial background component.

The three components have to be discriminated in the fit. This is possible, since the signal is expected to peak at the D^0 mass whereas the misidentified background is expected to peak at lower masses, because of the wrongly assigned electron masses to the pions. In contrast to that, the combinatorial background is not peaking.

The mass shapes for the signal and misidentified background are modeled by double-sided Crystal Ball (DSCB) functions [47]. These consist of an asymmetric Gaussian core and two power-law tails. For the signal, the tails describe energy loss due to missed bremsstrahlung photons for lower invariant masses and energy resolution effects in the bremsstrahlung photon reconstruction or wrongly added photons for higher invariant masses. For the mis-identified background, the DSCB function was chosen since the wrong mass hypothesis for the mis-identified pions and wrongly added bremsstrahlung photons distort the mass shape. The DSCB function has seven parameters and is defined as:

$$DSCB(m; m_0, \sigma_L, \sigma_R, \alpha_L, \alpha_R, n_L, n_R) = \begin{cases} A_L \cdot (B_L - \frac{m-m_0}{\sigma_L})^{-n_L} & \text{, for } \frac{m-m_0}{\sigma_L} < -\alpha_L \\ exp(-\frac{1}{2} \cdot (\frac{m-m_0}{\sigma_L})^2) & \text{, for } \frac{m-m_0}{\sigma_L} \leq 0 \\ exp(-\frac{1}{2} \cdot (\frac{m-m_0}{\sigma_R})^2) & \text{, for } \frac{m-m_0}{\sigma_R} \leq \alpha_R \\ A_R \cdot (B_R + \frac{m-m_0}{\sigma_R})^{-n_R} & \text{, otherwise.} \end{cases} \tag{6.1}$$

For $i \in \{L, R\}$, the normalization factors are given by:

$$A_i = (\frac{n_i}{|\alpha_i|})^{n_i} \cdot exp(-\frac{|\alpha_i|^2}{2}), \tag{6.2}$$

$$B_i = \frac{n_i}{|\alpha_i|} - |\alpha_i|. \tag{6.3}$$

Parameters with subscript L and R determine the shape to the left and right side of the peak, respectively. The parameters σ_L, σ_R and m_0 describe the widths and the mean of the asymmetric Gaussian. The transition points to the tails are given by α_L and α_R and the power-laws of the tails are determined by n_L and n_R.

The full event selection is applied to the simulated samples for $D^0 \to K^-\pi^+e^-e^+$ candidates and $D^0 \to K^-\pi^+\pi^-\pi^+$ candidates. The $D^0 \to K^-\pi^+\pi^-\pi^+$ sample is, in addition, reconstructed like the signal channel by assigning the electron mass hypothesis to two random, opposite charged pions. Both samples are split into the two bremsstrahlung categories and a total of four unbinned maximum likelihood fits are performed. The results of these fits are shown in figure 6.1. In each figure, a vertical green line indicates the PDG mass of the D^0 meson. The two signal peaks coincide with the D^0 mass, while the peak of the mis-identified $D^0 \to K^-\pi^+\pi^-\pi^+$ candidates is shifted to lower masses due to the wrong mass hypothesis. For the **brem1**+ sample, this shift is partly compensated by wrongly added bremsstrahlung photons to the pions. The fit parameters are given in the tables 6.1 and 6.2 for the bremsstrahlung categories **brem0** and **brem1**+, respectively.

The last component for the fits of the data samples is the combinatorial background. It is modeled by a linear function, parameterized by a first-order Chebyshev function C [48]. It is defined by:

$$C(m; a) = T_0(x) + T_1(x) \cdot a, \tag{6.4}$$

with the Chebyshev polynomials:

$$T_0(x) = 1, \quad T_1(x) = x. \tag{6.5}$$

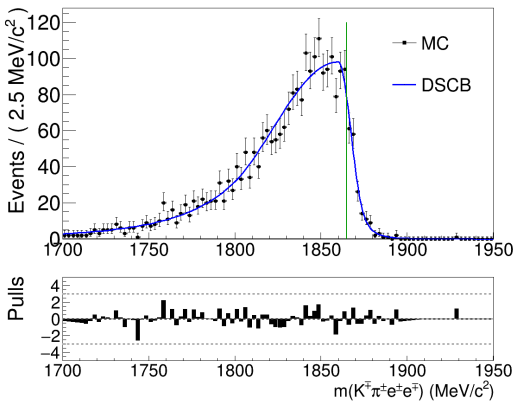

(a) $D^0 \to K^-\pi^+e^-e^+$: **brem0**

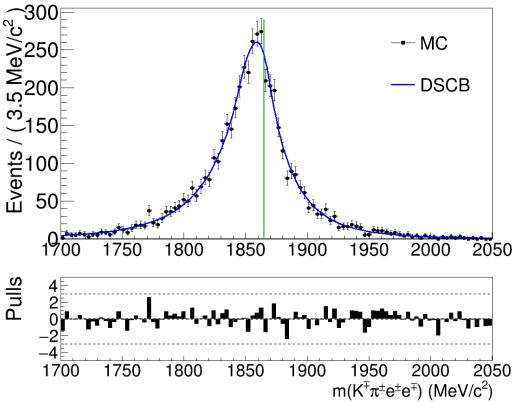

(b) $D^0 \to K^-\pi^+e^-e^+$: **brem1+**

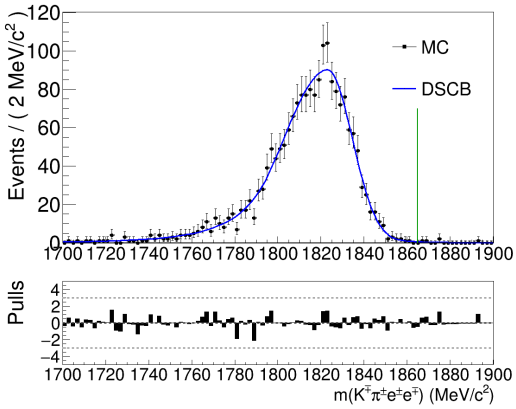

(c) $D^0 \to K^-\pi^+\pi^-\pi^+$: **brem0**

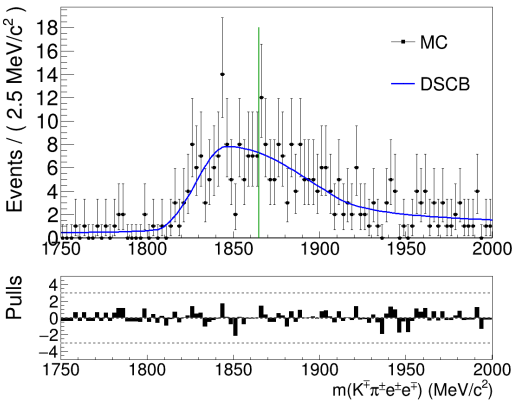

(d) $D^0 \to K^-\pi^+\pi^-\pi^+$: **brem1+**

Figure 6.1: Fit of the D^0 mass for the simulated samples of the signal channel. The top two plots are the signal candidates, the bottom two plots are the wrongly identified $D^0 \to K^-\pi^+\pi^-\pi^+$ candidates. The candidates in the **brem0** category are shown on the left, the candidates in the **brem1+** shown on the right. The D^0 mass is indicated with a green vertical line. Deviations between model and data for each fit are shown in a pull plot.

Parameter	Value for $D^0 \to K^-\pi^+e^-e^+$	Value for $D^0 \to K^-\pi^+\pi^-\pi^+$
m_0	1860 ± 1	1823 ± 1
σ_L	39 ± 3	20 ± 1
σ_R	7.3 ± 0.9	11.3 ± 0.7
α_L	1.3 ± 0.1	1.4 ± 0.2
α_R	1.8 ± 0.3	2.6 ± 0.3
n_L	6 ± 1	5 ± 3
n_R	5 ± 3	2 ± 1

Table 6.1: Parameters of the fits to the $D^0 \to K^-\pi^+e^-e^+$ and misidentified $D^0 \to K^-\pi^+\pi^-\pi^+$ MC samples with no added bremsstrahlung photons.

Parameter	Value for $D^0 \to K^-\pi^+e^-e^+$	Value for $D^0 \to K^-\pi^+\pi^-\pi^+$
m_0	1860 ± 2	1846 ± 4
σ_L	21 ± 4	18 ± 3
σ_R	14 ± 4	50 ± 5
α_L	0.8 ± 0.1	2.1 ± 0.4
α_R	0.7 ± 0.1	1.3 ± 0.4
n_L	6.0 ± 0.5	0.2 ± 0.7
n_R	6 ± 4	0.4 ± 0.6

Table 6.2: Parameters of the fits to the $D^0 \to K^-\pi^+e^-e^+$ and misidentified $D^0 \to K^-\pi^+\pi^-\pi^+$ MC samples with at least one added bremsstrahlung photon.

The full model M, used to describe the D^0 mass distribution of the $D^0 \to K^-\pi^+e^-e^+$ data sample for each bremsstrahlung category b, is given by:

$$M^b = N^b_{Sig} \cdot DSCB^b_{Sig} + N^b_{Bkg} \cdot DSCB^b_{Bkg} + N^b_{CombBkg} \cdot C^b_{CombBkg}, \tag{6.6}$$

where N_{sig}, N_{Bkg} and $N_{combBkg}$ are the yields for the signal, misidentified background and combinatorial background, respectively. The fit is performed simultaneously in both bremsstrahlung categories. The shape parameters of the signal and mis-identified background are fixed to the values obtained by the MC fits. Also, the number of misidentified background candidates in the **brem1+** category is fixed by the ratio r of events between both categories in the misidentified $D^0 \to K^-\pi^+\pi^-\pi^+$ MC fits. This ratio is given by:

$$r = \frac{N^{\mathbf{brem1+}}_{Bkg,MC}}{N^{\mathbf{brem0}}_{Bkg,MC}} = 0.160 \pm 0.007 \tag{6.7}$$

This is done to further improve the stability of the fit as the misidentified background shape lies directly under the signal peak in the **brem1+** category (see fig-

ures 6.1b and 6.1d). The shift due to wrongly associated masses for the pions is compensated by randomly added photons during the bremsstrahlung recovery. Therefore, only 4 parameters are free in this fit: The slope of the combinatorial background, the yield for the misidentified background in the **brem0** category and both signal yields. The fit results are shown in figure 6.2. In the lower part of the figures, corresponding pull plots are added. These show the differences between data points and model in units of their error. Most data points lie within 2σ of the model and there are no bigger regions, where the deviations are onesided, which means that the data is well described by the model. In the lower half of figure 6.5, the plot for category **brem1**+ is shown. For this sample, the background component from $D^0 \to K^-\pi^+\pi^-\pi^+$ decays (shown in yellow) is significantly suppressed. This is a result of the bremsstrahlung requirement as the bremsstrahlung photon(s) were randomly added to the pions and not emitted by them. The associated parameters for this fit are given in table 6.3. In total, 370 ± 30 (610 ± 40) signal events are found for the **brem0** (**brem1**+) category.

Parameter	Value for **brem0**	Value for **brem1**+
a	0.0 ± 0.2	-0.04 ± 0.07
N_{Bkg}	90 ± 20	-
$N_{CombBkg}$	150 ± 20	640 ± 40
N_{Sig}	370 ± 30	610 ± 40

Table 6.3: Parameters of the fits to the $D^0 \to K^-\pi^+e^-e^+$ data samples. N_{Bkg} for **brem1**+ is fixed by N_{Bkg} for **brem0** and the ratio of both categories obtained by the MC fit.

6.2 Normalization Channel

For the normalization channel $D^0 \to K^-\pi^+\pi^-\pi^+$, a similar approach is chosen to determine the event yield. After the selection, the data sample consists of two components:

- signal $D^0 \to K^-\pi^+\pi^-\pi^+$ events
- combinatorial background

Also for the normalization channel, the contribution of physical backgrounds is suppressed by the topological requirements in the selection. Other D^0 decays with four daughter particles have significantly lower branching fractions compared to $D^0 \to K^-\pi^+\pi^-\pi^+$, therefore, misidentified background from these decays is not expected.

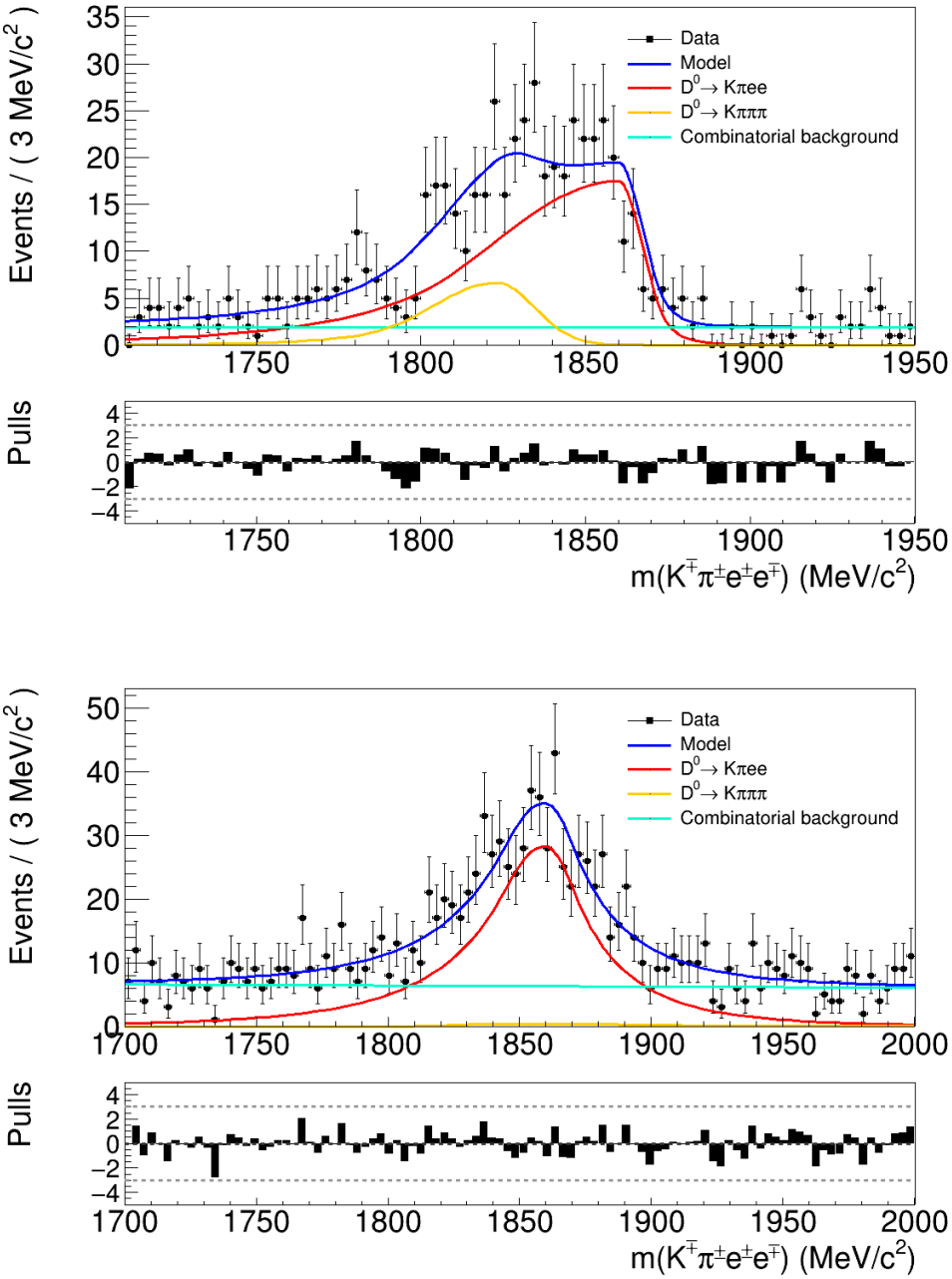

Figure 6.2: Fit of the D^0 mass for the data samples of the signal channel. The top plot shows the sample in the bremsstrahlung category with no added photon, the bottom plot shows the sample where at least one photon was added to the event candidate. The deviations between composite model (shown in blue) and data are shown as a pull plot.

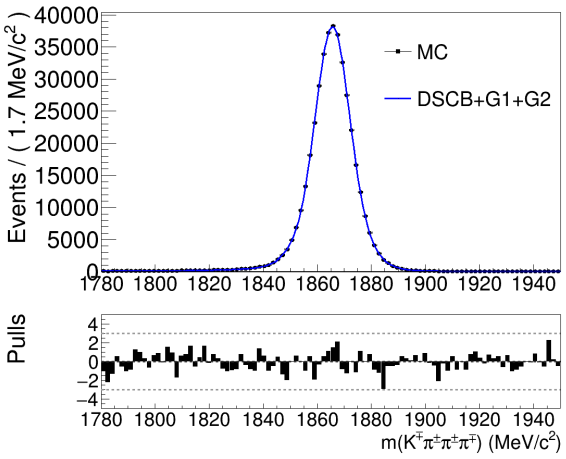

Parameter	Value for $D^0 \to K^-\pi^+\pi^-\pi^+$
m_0	1865.67 ± 0.06
σ_L	5.7 ± 0.1
σ_R	5.53 ± 0.10
α_L	2.14 ± 0.04
α_R	2.60 ± 0.05
n_L	0.89 ± 0.07
n_R	1.06 ± 0.09
$f1$	0.44 ± 0.01
m_{G1}	1865.76 ± 0.08
σ_{G1}	8.48 ± 0.09
$f2$	0.53 ± 0.01
m_{G2}	1861.2 ± 0.9
σ_{G2}	18.5 ± 0.9

Figure 6.3: Fit of the D^0 mass for the simulated samples of the normalization channel. The fit model is a DSCB function and two Gaussians. The corresponding values for the parameters are given in the table on the right.

The mass shape of the $D^0 \to K^-\pi^+\pi^-\pi^+$ candidates is more complex as the size of the samples is larger reducing the relative statistical errors per bin. This means simple models with only a few parameters cannot adequately describe the data. Therefore, the shape is modeled by the sum of a DSCB function and two Gaussian functions (G_1,G_2):

$$M_{Sig} = f_1 \cdot DSCB + f_2 \cdot G_1 + (1 - f_1 - f_2) \cdot G_2, \tag{6.8}$$

where f_1 and f_2 are the fractions of the total yield described by the DSCB function and the first Gaussian, respectively. There are no shared parameters between the three functions. As before, this shape is first fitted to the simulated sample with the full selection for the normalization channel applied. The resulting fit is shown in figure 6.3 together with the associated values of the parameters. For the full model of the data sample, an additional first-order Chebyshev function C describes the combinatorial background. The full model is given by:

$$M = N_{Sig} \cdot M_{Sig} + N_{CombBkg} \cdot C. \tag{6.9}$$

In the data sample, the huge statistics present a challenge when fitting the mass shape. As mentioned above, the relative error decreases for a higher number of events. This means that the model to describe the data has to be more accurate. On the other hand, possible differences between simulation and data are more significant, if the sample sizes increase. These two factors are the reason why the mass shape obtained in the MC fit does not fit well for data. Therefore, it is not possible

to fix the mass shape for the normalization channel, as it was done beforehand in the fits for the signal channel.

A possible approach to this problem is to perform a fit without any information from the MC sample, where all parameters are free. However, as the full model has many parameters, the free fit does not converge. The approach which was chosen is to use the MC fit to reduce the number of free parameters and stabilize the fit. This is done by introducing two parameters that alter the shape from the MC fit: A shift parameter m_{shift} that controls the position of the peak and a scale parameter t that controls the width. In the model from equation 6.9, m_{shift} is added to the means of the DSCB function and the two Gaussians, and the four width parameters are multiplied by t. In addition to that, the tail parameters of the DSCB function are restricted by adding four Gaussian constraints to the likelihood function of the fit. This prevents the signal shape from partly describing the combinatorial background component.

To additionally enforce the stability of the $D^0 \to K^-\pi^+\pi^-\pi^+$ fit, a data-driven approach was chosen to fix the shape of the combinatorial background. This is done with a wrong-sign data sample stemming from $D^0 \to K^+\pi^-\pi^+\pi^-$ decays, where the charges of the kaon and the first pion are opposite with respect to the normalization channel. In this sample, the signal to background ratio is much lower, which makes a suitable candidate for modeling the combinatorial background.

The same selection as as for the $D^0 \to K^-\pi^+\pi^-\pi^+$ sample (see chapter 5) is applied to the wrong-sign sample. All cuts that depend on the particle identity, e.g. the cuts on the PID variables, are adjusted accordingly. After obtaining the data sample, the mass distribution in the outer side-bands, where the signal peak has a minimal influence on the shape, is fitted using a first-order Chebyshev function with parameter a. The side-band for lower masses is defined from $1780\,\mathrm{MeV}/c^2$ to $1820\,\mathrm{MeV}/c^2$ and the side-band for higher masses is defined from $1910\,\mathrm{MeV}/c^2$ to $1950\,\mathrm{MeV}/c^2$. The result of this fit is shown in figure 6.4. The obtained value for a is:

$$a = 0.024 \pm 0.004 \tag{6.10}$$

The deviation between the data points and the fit are mostly under 3σ. However, there is a clear systematic trend visible showing that the fit shape can not fully describe the combinatorial background shape. A deviation of 2σ corresponds to ≈ 100 events per bin. In the right-sign sample, the number of expected combinatorial background events is in the same order of magnitude as in the wrong-sign sample. Therefore, the effect of the trend only has a small impact on the final fit. This can also be seen by the high sample purity in the peak region for the signal from 1850 to $1880\,\mathrm{MeV}/c^2$ of 98.8%.

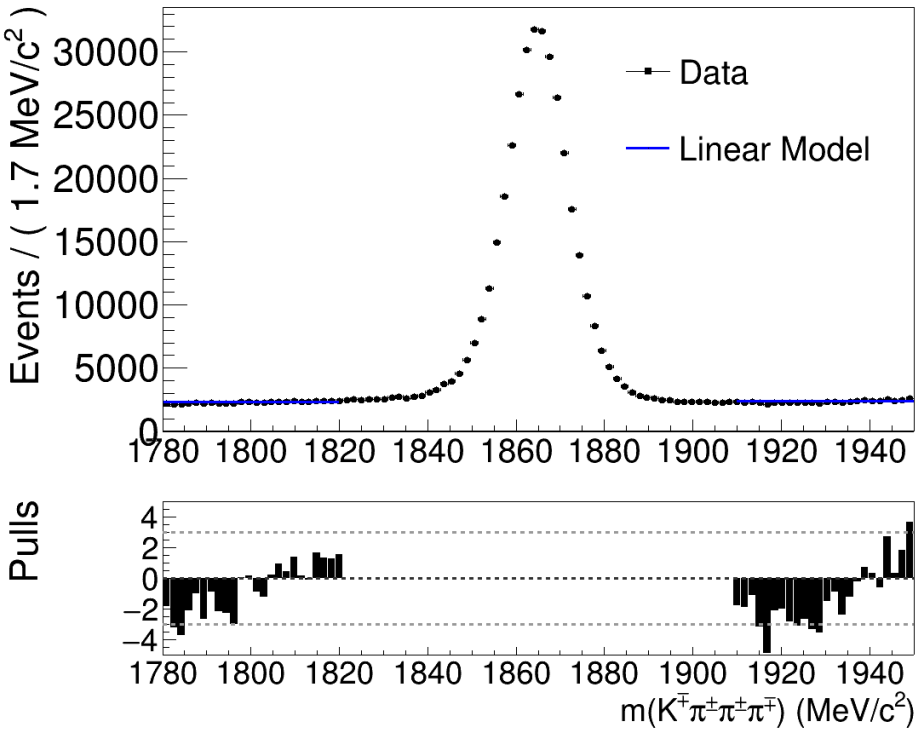

Figure 6.4: Fit to the side bands of the $D^0 \to K^+\pi^-\pi^+\pi^-$ data sample.

Parameter	Value for $D^0 \to K^-\pi^+\pi^-\pi^+$
m_{shift}	-0.839 ± 0.002
t	1.0241 ± 0.0003
α_L	2.195 ± 0.003
α_R	3.49 ± 0.02
n_L	0.682 ± 0.005
n_R	0.95 ± 0.06
N_{Sig}	13399000 ± 4000
$N_{CombBkg}$	647000 ± 3000

Table 6.4: Parameters of the fit to the $D^0 \to K^-\pi^+\pi^-\pi^+$ data sample.

With the results of the previous section, the model of equation 6.9 can be fitted to the data sample of the normalization channel. This is done with a binned maximum likelihood fit. The results are shown in figure 6.5. The associated parameters for this fit are given in table 6.4. In total 13399000 ± 4000 events are found.

In the lower part of the plot, the pulls and residuals are shown. Even though the shape of the mass peak is only constrained by the shape of the MC fit, in some bins, the model and data points deviate up to a few percent. However, it is not necessary to describe the mass shape perfectly as long as the error of the total number of events is small. The reason for this is that only the final event yield enters the branching fraction formula. When summing over the residuals, the total error is as large as the error for the sum of the total event numbers from the fit. The relative error for the number of events in the normalization channel is 0.03%. This is small in comparison to the signal channel, where the relative errors lie between 5 and 10%. Therefore, the uncertainties on the branching fraction introduced by the mismatched mass shape is neglectable.

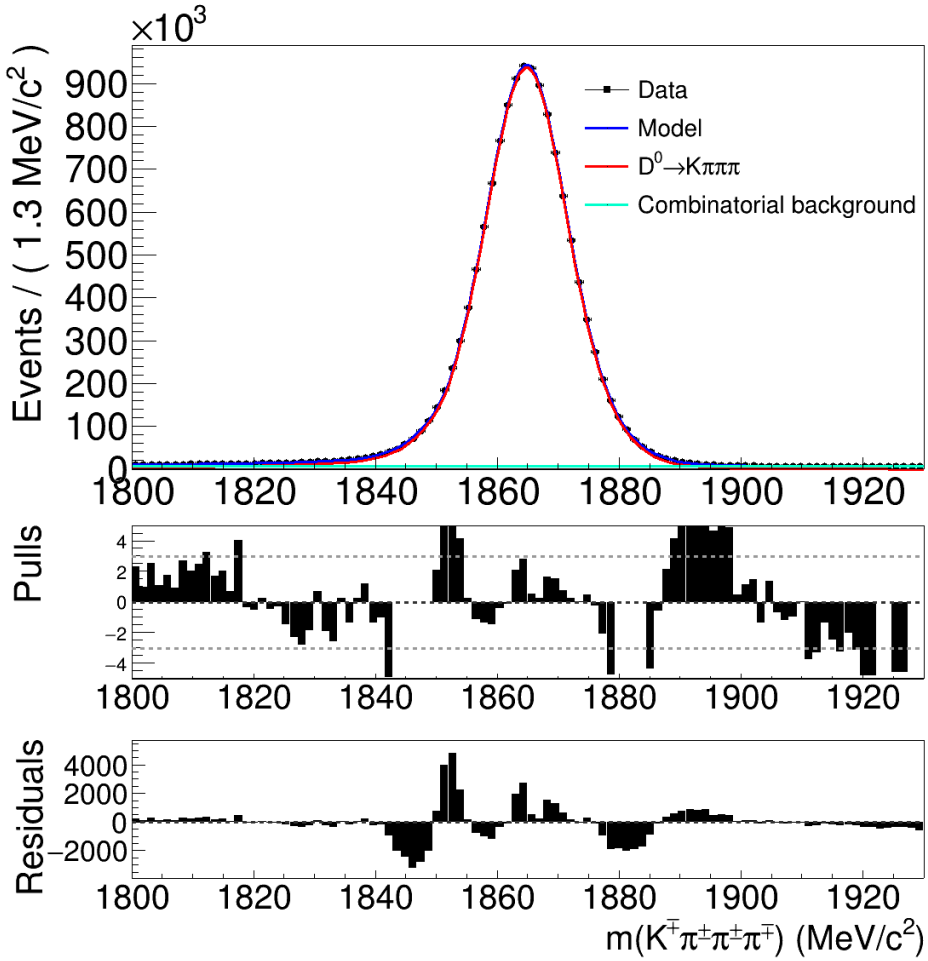

Figure 6.5: Fit of the D^0 mass for the data samples of the normalization channel. Due to large statistics and therefore small statistical uncertainties in the data points, a plot of the residuals is shown in addition to the pull plot. Because of shape differences between data and MC, the fit model is only constrained by the MC fit.

7 Efficiencies

Only a fraction of all events that occurred during data taking can be detected and remain after the selection process. This is accounted for by the total efficiency. To accurately determine the branching fraction, the efficiencies of both signal and normalization channel have to be evaluated.

7.1 Efficiency Estimation

The normalization channel is chosen to be similar to the signal in terms of the event topology and number of final state particles. If the efficiencies were equal for both decays, their ratio in the formula for the branching fraction would be one and could be neglected all together. However, this is not the case, since electrons and pions differ quite significantly. First of all, they are detected and measured by different sub-detectors. While the electrons are measured by the ECAL, the pions are measured by the HCAL. Secondly, the accessible phase space is different for both kinds of particles, because they differ in mass. On top of that, electrons can emit bremsstrahlung when interacting with the material inside the detector. In these cases, the emitted bremsstrahlung photons have to be detected and correctly matched to the event. Apart from these differences both channels should be similar enough so that most efficiencies (e.g. tracking efficiency) and the resulting systematic uncertainties cancel in the ratio. The efficiencies are determined using the simulated event samples, since for them the number of generated signal events is known and they are background free. To be able to estimate the efficiencies for data, the simulated samples run through the same selection process. The total efficiency is factorized into several partial efficiencies:

$$\epsilon = \epsilon_{acc,rec} \times \epsilon_{sele} \times \epsilon_{PID} \times \epsilon_{Trig} \tag{7.1}$$

where $\epsilon_{acc,rec}$ is the acceptance and reconstruction efficiency, ϵ_{sele} is the selection efficiency , ϵ_{PID} is the efficiency of the PID cut and ϵ_{Trig} is the efficiency of the trigger.

The acceptance and reconstruction efficiencies are put together into one category as the event generation is different for the signal and normalization channel. In the $D^0 \to K^-\pi^+\pi^-\pi^+$ MC sample, strict cuts at earlier stages were applied to further reduce the sample size to save computational resources in the reconstruction. This results in an increased reconstruction efficiency. Therefore, the acceptance

and reconstruction efficiencies for the signal and normalization channel can not be compared individually. The trigger efficiencies are determined after the events have passed all selection criteria apart from the L0 and HLT1 trigger. This is done to save computational resources.

7.2 Acceptance

The acceptance efficiencies include the acceptance of the detector as well as applied generator level and filter cuts for the normalization channel. They are taken out of summary tables that are produced by the simulation software. The resulting efficiencies are given in table 7.4.

7.3 Reconstruction

The simulation does not perfectly describe the tracking efficiency. Therefore, the reconstruction efficiency, that is obtained from the simulated samples, has to be corrected. A standard procedure for this is to use so called tracking efficiency maps. These contain correction weights for MC events in different kinematic bins. To calculate the correction weights, calibration data samples and corresponding simulated samples of $J/\psi \to \mu^+\mu^-$ decays were used. Furthermore, this analysis uses dedicated maps for the electron reconstruction, calculated with $J/\psi \to e^+e^-$ decay samples. The electron maps were produced in a recent LHCb analysis, where $B^+ \to K^+\ell^+\ell^-$ and $B^0 \to (K^{*0} \to)K^+\pi^-\ell^+\ell^-$ decays were studied [49, 50]. The additional electron maps were used to account for differences between muon and electron reconstruction. These stem, for example, from the bremsstrahlung recovery algorithms in the electron reconstruction.

For each kinematic bin, the reconstruction efficiencies for data and simulation are calculated by a tag-and-probe method. The weight for a bin is then given by the efficiency ratio. This is done for muons and electrons separately, resulting in two different kinds of tracking maps. As they are both long lived charged particles, the muon maps are used to correct for the tracking of hadrons. They are binned in momentum p and pseudorapidity η. The bin edges are defined as:

- $p = [5000, 10000, 20000, 40000, 100000, 200000]\,\mathrm{MeV}/c$
- $\eta = [1.9, 3.2, 4.9]$

The electron maps are binned in transverse momentum p_T, pseudorapidity η and the azimuthal angle ϕ. The bin edges are defined as:

- $p_T = [150, 490, 520, 550, 657, 760, 780, 785, 865, 915, 1065, 1245, 1300,$
  $1475, 1600, 1950, 2000, 2430, 3020, 4000, 4310, 5810, 50000]\,\mathrm{MeV}/c$

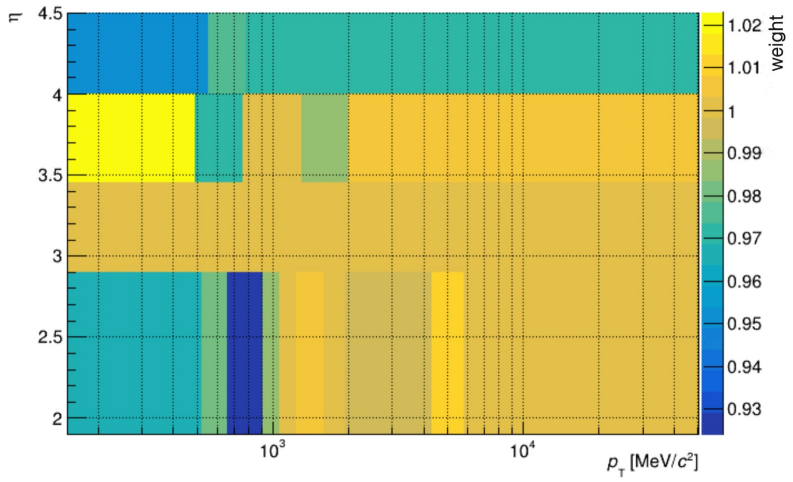

Figure 7.1: Electron tracking map for 2017. The correction weights shown are given in bins of p_T and η for the central ϕ bin.

- $\eta = [1.9, 2.9, 3.45, 4, 4.5]$
- $\phi = [-\pi, -\frac{5}{8}\pi, -\frac{3}{8}\pi, \frac{3}{8}\pi, \frac{5}{8}\pi, \pi]$.

An example of an electron tracking map is shown in figure 7.1. For large fractions of the phase space, the MC describes the data well and the ratio between data and MC efficiency results in 1 corresponding to no correction.

The tracking maps are given separately for each year of data taking. For the MC sample of the signal decay, $D^0 \to K^-\pi^+e^-e^+$, four correction factors for the four daughter particles, K^-, π^+, e^+ and e^-, are calculated for the years 2017 and 2018 separately. The correction factor for a hadron is calculated in the following way: The number of simulated events in bins of p_T and η, $N_{had}(p_T, \eta)$, is multiplied with the corresponding weight, $\omega_{muon}(p_T, \eta)$, of the tracking map. The index *had* stands for one of the two hadron decay daughters, the pion or the kaon. The correction factor α_{had} is obtained by summing over all bins and dividing by the total number of simulated events before the reconstruction N_{before}:

$$\alpha_{had} = \sum_{p_T,\eta} N_{had}(p_T, \eta) \cdot \omega^i_{muon}(p_T, \eta) \Big/ N_{before}, \quad had \in \{\pi^-, K^+\}. \tag{7.2}$$

This is done for all hadron decay daughters. The tracking maps for electrons are additionally binned in ϕ, resulting in:

$$\alpha_e = \sum_{p_T,\eta,\phi} N_e(p_T, \eta, \phi) \cdot \omega_{elec}(p_T, \eta, \phi) \Big/ N_{before}, \quad e \in \{e^+, e^-\}. \tag{7.3}$$

where $N_e(p_T, \eta, \phi)$ is the number of events in one bin and $\omega_{elec}(p_T, \eta, \phi)$ the corresponding weight for this bin. The final corrected number of simulated events, N_{corr}, is calculated by multiplying the selected number of events by all four correction factors:

$$N_{corr} = N \cdot \alpha_{K^-} \cdot \alpha_{\pi^+} \cdot \alpha_{e^+} \cdot \alpha_{e^-}. \tag{7.4}$$

This is done for the MC sample for each year separately. Finally, the corrected event counts are summed up over the years. The corrected reconstruction efficiency is obtained by dividing the corrected number of simulated events by the number of simulated events before reconstruction, N_{acc}:

$$\epsilon_{rec,corr} = \frac{\sum_{y=2017,2018} N^y_{corr}}{N_{acc}}. \tag{7.5}$$

For the MC sample of the normalization channel, $D^0 \to K^-\pi^+\pi^-\pi^+$, the reconstruction efficiency is corrected the exact same way, but only the muon maps are needed. The effect of the efficiency correction can be seen in table 7.1, where the corrected and uncorrected reconstruction efficiencies are given. The uncorrected efficiencies are calculated by simply dividing the number of reconstructed events by the number of events before reconstruction. For both decay channels, the correction is in the order of 2 to 3%. The correction of the ratio of the efficiencies between the two channels is smaller, resulting in a relative correction of 0.2%.

ϵ_{rec}	$D^0 \to K^-\pi^+e^-e^+$	$D^0 \to K^-\pi^+\pi^-\pi^+$	$\frac{D^0 \to K^-\pi^+\pi^-\pi^+}{D^0 \to K^-\pi^+e^-e^+}$
uncorrected	0.00693 ± 0.00002	0.99450 ± 0.00002	143.5
corrected	0.00675 ± 0.00002	0.97085 ± 0.00004	143.8

Table 7.1: Effect of the reconstruction efficiency correction.

Compared to leptons, hadrons are subject to hadronic interactions with the detector material and a fraction of them is lost in the reconstruction. This needs to be taken into account, especially since the normalization channel has two additional final state hadrons. Hadronic interactions are part of the systematic uncertainty of the reconstruction efficiency and are accounted for in chapter 8.1.

7.4 Selection

The selection efficiency is directly determined by the simulated samples using the number of events before (N_{before}) and after (N_{after}) the selection:

$$\epsilon_{sele} = \frac{N_{after}}{N_{before}}. \tag{7.6}$$

The number of events before the selection is taken before the HLT2 trigger condition is applied. Therefore, the trigger efficiency of HLT2 is included in the selection efficiency. The PID cuts on the final state particles are not included in the selection efficiency. They are evaluated in the next section. For the signal channel, the selection efficiency is evaluated separately for the two bremsstrahlung categories to account for differences in candidates with at least one added bremsstrahlung photon and none. The resulting selection efficiencies are given in table 7.4.

7.5 Particle Identification

The efficiency of the PID cut in the selection evaluated from the simulated samples does not match to the efficiency for data. Therefore, the MC samples need to be corrected such that they can be used for the PID efficiency. Using the samples before the PID cut is applied, a new PID response is calculated for each particle. This is done with the PIDGen2 software package [51, 52]. It uses calibration data samples with known PID to correct MC PID variables. This can be done by two different approaches: New variables that replace the PID response can be re-sampled or the variables of the PID response can be transformed that their distribution matches the data.

This analysis uses the re-sampling approach. The PID response depends on information on the track kinematics and the event multiplicity. Therefore, the event multiplicity, the kinematics of the particles in the calibration data samples, and the corresponding PID response are used to create calibration probability density functions (PDFs) for each particle type. Afterwards these PDFs are used to re-sample new PID responses for each particle of the simulated samples. For the electrons, calibration samples from $B^0 \to (J/\psi \to) e^+e^-$ decays are used. These are available for both bremsstrahlung categories such that a destinction between the categories can be made and the re-sampling is more accurate. The PID variables of the pions and kaons are re-sampled using calibration data from $D^{*+} \to \pi^+(D^0 \to) K^-\pi^+$ decays.

First, the particles with known PID are divided into a fine-binned four dimensional histogram: The momentum, p, transverse momentum, p_T, the number of tracks in the event, and the PID variable is used. In the second step, these histograms are smoothed. This is done to approximate the true, unbinned, continous PDF. Using a multidimensional gaussian filter algorithm, the bin entries are modified according to the entries of neighboring bins. The width of the kernel used for this operation determines how many neighbors are used and thus how much the histogram is smoothed. The resulting smoothed histograms of the calibration data are then used as PDFs to re-sample the PID response for the simulated samples according to the kinematic distribution of the tracks (p, p_T) and the event multiplicity.

After re-sampling the PID variables, the cut on these variables is performed and the resulting efficiencies are calculated as the ratio of the number of events before

and after the cut. As mentioned in chapter 5, the stripping lines apply loose PID requirements for the kaon and electron (see table 5.1). However, these are not corrected as there is no sample available, where no cut is applied.
In table 7.2, corrected and uncorrected PID efficiencies are shown together with the efficiency ratios between normalization and signal channel for both bremsstrahlung categories. The individual efficiencies are corrected by 4 to 8% with respect to their original value. The PID efficiency ratio correction is in the order of 0.7% (4%) for the **brem0** (**brem1**+) category.

ϵ_{PID}	$D^0 \to K^-\pi^+e^-e^+$		$D^0 \to K^-\pi^+\pi^-\pi^+$	$\frac{D^0\to K^-\pi^+\pi^-\pi^+}{D^0\to K^-\pi^+e^-e^+}$	
	brem0	**brem1**+		**brem0**	**brem1**+
uncorrected	0.454 ± 0.005	0.508 ± 0.004	0.6739 ± 0.0004	1.484	1.327
corrected	0.475 ± 0.005	0.550 ± 0.004	0.7002 ± 0.0004	1.474	1.273

Table 7.2: Effect of the PID efficiency correction.

7.6 Trigger

Similar to the tracking and the PID response, the trigger response is not well described by the simulation. Therefore, the trigger efficiencies of the MC samples are corrected using the result of the TISTOS method applied to data as described in chapter 4. For this, calibration samples for data and MC from $B^0 \to K^{*0}J/\psi$ decays are used to calculate correction factors. These decays are chosen as they have a similar event topology to the studied D^0 decays. The selection used for these samples is taken from the aforementioned study of $B^+ \to K^+\ell^+\ell^-$ and $B^0 \to (K^{*0} \to)K^+\pi^-\ell^+\ell^-$ decays [49, 50].

In the L0 trigger stage, the trigger decision depends on single particle signatures. Thus, the L0 triggers are evaluated separately for each particle. The correction is done in kinematic bins of momentum p and transverse momentum p_T of the respective particle. The bin edges are defined as follows:

- $p_T = [0, 550, 750, 1000, 1250, 1600, 2000, 2800, 20000]\,\mathrm{MeV}/c$
- $p = [0, 15000, 10000000]\,\mathrm{MeV}/c$

For all L0 triggers, $B^0 \to (K^{*0} \to)K^+\pi^-(J/\psi \to)e^+e^-$ decays are used. The hadron triggers are additionally evaluated using $B^0 \to (K^{*0} \to)K^+\pi^-(J/\psi \to)\mu^+\mu^-$ decays.

The L0 trigger condition for the TIS samples is defined as an OR between the *HadronDecision_ TIS* for the pion and the kaon, and the *ElectronDecision_ TIS* and *MuonDecision_ TIS* for the electrons. However, since the TIS condition has to be

independent of the evaluated TOS decision, correlated triggers are left out. This results in the following TIS conditions for L0 trigger of the pion, kaon and first electron, respectively:

- `Pi_TIS = Pi_Hadron_TIS OR E1_Muon_TIS OR E1_Electron_TIS OR E2_Muon_TIS OR E2_Electron_TIS`
- `K_TIS = K_Hadron_TIS OR E1_Muon_TIS OR E1_Electron_TIS OR E2_Muon_TIS OR E2_Electron_TIS`
- `E1_TIS = Pi_Hadron_TIS OR K_Hadron_TIS OR E1_Muon_TIS OR E1_Electron_TIS OR E2_Muon_TIS`

For the second electron, the TIS condition is similar to the one for the first electron. The condition for the TISTOS sample is now defined as an AND between the TOS condition of the investigated trigger and the corresponding TIS condition. For example, the TISTOS condition for the pion L0 trigger is defined as:

- `Pi_TISTOS = Pi_Hadron_TOS AND Pi_TIS`.

The two triggers in the HLT1 stage are evaluated at the same time since they trigger on the D^0 meson. They are evaluated in kinematic bins of momentum p and transverse momentum p_T of the D^0 meson. The bin edges are given by:

- $p_T = [0, 4000, 6000, 8000, 10000, 12000, 13000, 15000, 17000, 19000, 50000]\,\mathrm{MeV}/c$
- $p = [0, 100000, 10000000]\,\mathrm{MeV}/c$

The correction factors are calculated using $B^0 \to (K^* \to)K^+\pi^-(J/\psi \to)e^+e^-$ decays. Thus, the B^0 and the D^0 mesons have the same daughter particles. The trigger conditions for the TIS and TISTOS samples are defined as:

- `HLT1_TIS = B0_HLT1Phys_TIS`
- `HLT1_TISTOS = (B0_HLT1TrackMVA_TOS OR B0_HLT1TwoTrackMVA_TOS) AND B0_HLT1Phys_TIS`

After defining the trigger conditions for the TIS and TISTOS samples, all trigger efficiencies of the data and MC candidates are calculated for each year of data taking individually for the calibration samples. In case of the electron triggers, the trigger efficiency is separately estimated for both bremsstrahlung categories. The efficiency is calculated by dividing the number of candidates passing the TISTOS condition by the number of candidates passing the TIS condition in their corresponding kinematic bins.

The correction factor ω_j for kinematic bin j is given by the ratio of the efficiencies for data and MC:

$$\omega_j = \frac{\epsilon_j^{data}}{\epsilon_j^{MC}}. \tag{7.7}$$

If a certain bin is empty for MC or data, no correction is applied. The correction factors for the L0 kaon trigger calculated are shown in figure 7.2. The calibration samples from $B^0 \to (K^* \to) K^+\pi^-(J/\psi \to) e^+e^-$ decays contain significantly less candidates compared to the samples from $B^0 \to (K^* \to) K^+\pi^-(J/\psi \to) \mu^+\mu^-$ decays. Therefore, the statistical uncertainties of the correction factors are higher. The correction factors obtained by the two calibration samples are compatible within their respective statistical uncertainties. For the trigger correction, the factors obtained by the $B^0 \to (K^* \to) K^+\pi^-(J/\psi \to) \mu^+\mu^-$ samples are chosen to decrease the impact of the statistical uncertainty introduced by the calibration samples. The remaining correction factors for the trigger efficiencies can be found in appendix A. Similarly to the kaon trigger, also the L0 pion trigger correction is done with the factors obtained from the $B^0 \to (K^* \to) K^+\pi^-(J/\psi \to) \mu^+\mu^-$ sample to decrease the impact of the statistical uncertainty.

The trigger efficiencies of the $D^0 \to K^-\pi^+e^-e^+$ and $D^0 \to K^-\pi^+\pi^-\pi^+$ decays are evaluated by applying the correction factors to the MC samples of both decays correcting for differences between MC and data. The correction is done individually for each year of data taking and in the signal channel for both bremsstrahlung categories. First, the total number of simulated candidates before the L0 and HLT1 triggers are applied, $N^{y,b}_{before}$, is determined. The variable y denotes the year and b the bremsstrahlung category in case of the signal channel. After applying the trigger conditions, they are sorted into the same kinematic bins as the correction weights. This results in two dimensional histograms with bins of p and p_T. This is done for the D^0 meson (HLT1) and all four decay daughters (L0). In the next step, the number of events in each bin is multiplied by its corresponding correction factor. This procedure is equivalent to the reconstruction efficiency correction. Summing over the bins results in the corrected number of simulated events after the trigger condition, $N^{y,b}_{after}$. The corrected trigger efficiency is obtained by summing over the years and dividing both event counts:

$$\epsilon^b_{corr} = \frac{\sum_{y=2017,2018} N^{y,b}_{after}}{\sum_{y=2017,2018} N^{y,b}_{before}} \tag{7.8}$$

The corrected and uncorrected trigger efficiencies can be found in table 7.3. The individual efficiencies are corrected by 45 to 60% with respect to their original value. The efficiency ratio correction of the normalization and signal channel with no added bremsstrahlung photons is in the order of 20%. The ratio for the other

bremsstrahlung category is 38% higher than before the correction. The trigger response of the detector is not well described by the simulation. This was also seen in other analyses [49, 50].

ϵ_{Trig}	$D^0 \to K^-\pi^+e^-e^+$		$D^0 \to K^-\pi^+\pi^-\pi^+$	$\frac{D^0\to K^-\pi^+\pi^-\pi^+}{D^0\to K^-\pi^+e^-e^+}$	
	brem0	**brem1+**		**brem0**	**brem1+**
uncorrected	0.553 ± 0.007	0.507 ± 0.005	0.5586 ± 0.0006	1.01	1.10
corrected	0.254 ± 0.006	0.203 ± 0.004	0.3085 ± 0.0005	1.21	1.52

Table 7.3: Effect of the Trigger efficiency correction.

7.7 Final Efficiencies

The total efficiencies are calculated by multiplying all partial efficiencies. Table 7.4 gives an overview over all partial and the total efficiencies. Furthermore, the acceptance and reconstruction efficiencies are combined in the third line for a better comparison between the signal and normalization channel.
The total efficiencies are in the same order of magnitude for the signal and the normalization channel. This comes from the fact that the normalization channel has higher PID and acceptance/reconstruction efficiencies which is compensated by the lower selection efficiency. However, in the final branching ratio calculation, the prescale for the normalization channel has to be considered. This decreases the efficiency of the normalization by a factor of 2.

Efficiency	$D^0 \to K^-\pi^+e^-e^+$		$D^0 \to K^-\pi^+\pi^-\pi^+$
	brem0	**brem1+**	
Acceptance	0.1832 ± 0.0003		0.002624 ± 0.000003
Reconstruction	0.00675 ± 0.00002		0.97085 ± 0.00004
Acc. & Rec.	0.001237 ± 0.000004		0.002548 ± 0.000003
Selection	0.190 ± 0.002	0.190 ± 0.002	0.05814 ± 0.00006
PID	0.475 ± 0.005	0.550 ± 0.004	0.7002 ± 0.0004
Trigger	0.254 ± 0.006	0.203 ± 0.004	0.3085 ± 0.0005
Total	$2.83(8) \times 10^{-5}$	$2.62(6) \times 10^{-5}$	$3.199(8) \times 10^{-5}$

Table 7.4: Overview of the total efficiencies with statistical errors of the MC sample sizes. The errors are calculated as binomial errors. In addition, for the normalization channel, the prescale factor (2) needs to be considered.

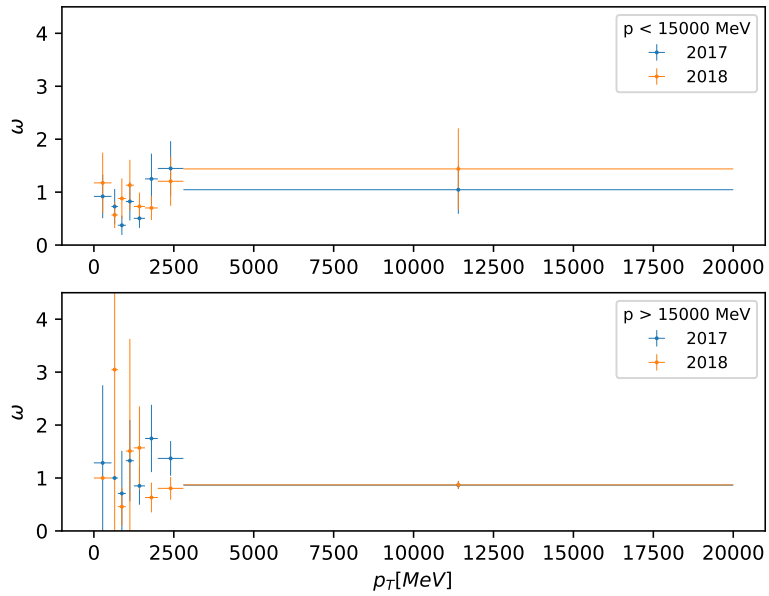

(a) $B^0 \to K^+\pi^-e^+e^-$ decays

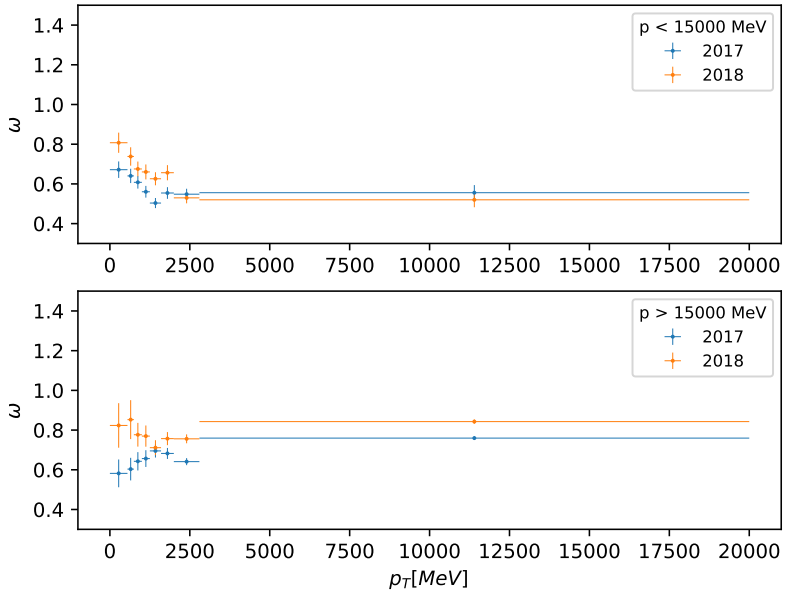

(b) $B^0 \to K^+\pi^-\mu^+\mu^-$ decays

Figure 7.2: L0 Trigger correction factors for kaons calculated with $B^0 \to (K^* \to)K^+\pi^-(J/\psi \to)e^+e^-$ decays (top) and $B^0 \to (K^* \to)K^+\pi^-(J/\psi \to)\mu^+\mu^-$ decays (bottom). The factors are given in kinematic bins of p_T and p. The factors for the lower momentum bin is shown in the upper plots, the factors for the upper momentum bin are in the lower plots, respectively. The different years of data-taking are shown in different colors.

8 Systematic Uncertainties

The main systematic uncertainties are related to the finite MC sample size and related to the various efficiency corrections. In this thesis, six systematic uncertainties related to the reconstruction, PID and MC sample size are estimated. Additionally, the systematic uncertainty arising due to the trigger correction was studied.

8.1 Reconstruction

Two types of systematic uncertainties in the reconstruction are studied. First, uncertainties due to interactions between hadrons and nuclei in the detector material. Hadrons produce showers that are absorbed in the detector material. If these interactions take place before the hadron has traversed the tracking system, it can not be reconstructed and is lost. The fraction of hadrons lost because of this effect was simulated for $B^0 \to J/\psi(K^{*0} \to)K^+\pi^-$ decays and is about 14% for pions and 11% for kaons [53]. This is accounted for in the simulation of the reconstruction. However, the material-budget of the detector has a relative uncertainty of 10%. This means that the reconstruction efficiencies for the pions (kaons) have an additional systematic uncertainty of 1.4%(1.1%).

The second systematic uncertainty stems from the tracking maps used for the efficiency correction. Each map has an intrinsic systematic uncertainty of 0.8% arising from differences in the efficiency ratio between MC and data when re-weighting the MC [54] [1].

The kinematic distributions for the kaon and the pion in the signal and normalization channel are very similar. Therefore, systematic uncertainties for these two particles are assumed to cancel in the final efficiency ratio. Thus, only the other two decay daughters of the D^0 have to be considered to calculate the systematic uncertainty of the reconstruction efficiency. Table 8.1 provides an overview of the uncertainties for the efficiency ratio for the individual particles. Since electrons are leptons and do not undergo hadronic interactions, the uncertainty coming from hadronic interactions for the ratio between pion and electron is just the 1.4% stated above. The tracking maps uncertainties are added quadratically, since the different maps for pions and electrons are considered to be uncorrelated. The efficiency is a product of all partial efficiencies, the total uncertainty for each source is obtained by quadratically adding the uncertainties of the single particle ratios. Thus, the

[1] The systematic uncertainty of 0.4% given in [54] was calculated for Run 1 data. The uncertainty for the tracking efficiency maps used in this analysis was determined analogously.

uncertainty coming from the hadronic interactions is $2\% = 1.4\% \bigoplus 1.4\%$ and the uncertainty of the tracking map correction is $1.6\% = 0.8\% \bigoplus 0.8\% \bigoplus 0.8\% \bigoplus 0.8\%$ relative to the total branching fraction.

Signal channel vs. normalization channel	Hadronic interactions	Tracking maps
K vs. K	-	-
π vs. π	-	-
e vs. π	1.4%	1.1%
e vs. π	1.4%	1.1%
Total	2.0%	1.6%

Table 8.1: Systematic uncertainties of the reconstruction efficiency.

8.2 Particle Identification

The systematic uncertainty of the PID correction process is given due to two different aspects of the correction method described in chapter 7.5: The finite size of the calibration samples and the smoothing procedure.

Statistical re-sampling is used to determine the influence of the sample size on the final result. Random events are drawn from the calibration sample to produce a sample of the same size. The events, which are chosen, are not removed from the original sample, such that it is possible that some events get chosen multiple times while others do not end up in the new sample. This re-sampling process is also called *bootstrapping* [55]. By this method, two additional calibration samples are produced and the PID correction is repeated. The resulting corrected efficiencies for these calibration samples are denoted with *default1* and *default2*.

Secondly, the Gaussian smearing is redone for the original calibration samples using a wider and a narrower kernel, denoted with *wide* and *narrow*, respectively. The results of the original re-sampling are denoted with *default*.

The PID efficiencies and their statistical errors of all five re-sampling instances are given in table 8.2. The variation introduced by the bootstrapping method is smaller as the statistical uncertainty of the efficiency and therefore neglected. In comparison to the different smearing kernels, the differences with respect to the *default* efficiency are larger than the statistical errors. The relative differences of the efficiency ratio are between 0.27 and 2.7% for the **brem0** category and between 0.24 and 0.94% for the **brem1+** category. The highest differences are with respect to the *narrow* efficiencies. These are in the same order compared to the statistical uncertainties of the efficiency ratio. The highest relative differences of the efficiency ratio for each bremsstrahlung category are used as final estimate for the systematic uncertainty for the PID correction.

ϵ_{PID}	$D^0 \to K^-\pi^+e^-e^+$		$D^0 \to K^-\pi^+\pi^-\pi^+$	$\frac{D^0 \to K^-\pi^+\pi^-\pi^+}{D^0 \to K^-\pi^+e^-e^+}$	
	brem0	**brem1+**		**brem0**	**brem1+**
default	0.475 ± 0.005	0.550 ± 0.004	0.7002 ± 0.0004	1.474 ± 0.016	1.273 ± 0.009
default1	0.474 ± 0.005	0.550 ± 0.004	0.7004 ± 0.0004	1.478 ± 0.016	1.273 ± 0.009
default2	0.474 ± 0.005	0.551 ± 0.004	0.7004 ± 0.0004	1.478 ± 0.016	1.271 ± 0.009
wide	0.460 ± 0.005	0.538 ± 0.004	0.6833 ± 0.0004	1.485 ± 0.016	1.270 ± 0.009
narrow	0.465 ± 0.005	0.548 ± 0.004	0.7042 ± 0.0004	1.514 ± 0.016	1.285 ± 0.009

Table 8.2: PID efficiencies for different calibration samples and Gaussian smearing. The errors are calculated according to the binomial error of the sample sizes. In the right column, the efficiency ratios with propagated errors are given.

8.3 Trigger

The uncertainty on the corrected trigger efficiency is estimated using the statistical uncertainty on the individual correction factors. For this, the correction is done two additional times. First, all factors are increased by their respective uncertainty, 1 sigma, and they are applied to the MC samples in the same way as before. Afterwards, the efficiency is calculated. This is then repeated using weights that are decreased by their respective 1 sigma uncertainty. This way, an estimate on the systematic uncertainty introduced by the correction factors is obtained. The resulting trigger efficiencies are shown in table 8.3. The efficiency ratio of normalization and signal channel differs between 17 and 27% for the **brem0** category and between 16 and 28% for the **brem1+** category compared to the ratio with original correction factors. For both categories, the larger difference is used as relative uncertainty related to the trigger efficiency ratio. These large differences have multiple causes. Firstly, by this method, all uncertainties are treated as totally correlated with each other as they are adjusted in the same direction. This leads to maximally increased or decreased trigger efficiencies, respectively. Additionally, the correction factors for the electrons have significantly larger statistical uncertainties compared to the correction factors for the hadrons due to smaller calibration sample sizes. As only the signal channel uses electron triggers, the signal trigger efficiencies change particularly strongly by varying the correction weights. This results in large differences in the efficiency ratio. Therefore, the systematic uncertainty due to the trigger correction is probably overestimated by this method.

8.4 Overview

An overview over all systematic uncertainties studied in this thesis is given in table 8.4. They are calculated relative to the efficiency ratio between normalization and signal channel separately for both bremsstrahlung categories. In addition to the uncertainties evaluated in this chapter, the statistical uncertainties due to the size

ϵ_{Trig}	$D^0 \to K^-\pi^+e^-e^+$		$D^0 \to K^-\pi^+\pi^-\pi^+$	$\frac{D^0\to K^-\pi^+\pi^-\pi^+}{D^0\to K^-\pi^+e^-e^+}$	
	brem0	**brem1+**		**brem0**	**brem1+**
ω	0.254 ± 0.006	0.203 ± 0.004	0.3085 ± 0.0005	1.21 ± 0.03	1.52 ± 0.03
$\omega + \sigma$	0.384 ± 0.007	0.301 ± 0.005	0.3821 ± 0.0006	1.00 ± 0.02	1.27 ± 0.02
$\omega - \sigma$	0.160 ± 0.005	0.127 ± 0.003	0.2458 ± 0.0005	1.54 ± 0.05	1.94 ± 0.05

Table 8.3: Trigger efficiencies and efficiency ratios for different correction factors. The factors are increased and decreased by their respective uncertainty.

of the MC samples is determined using the results of table 7.4. These could be reduced by increasing the computing resources spend on the simulation. To obtain the total relative uncertainty of the efficiency ratio, the uncertainties are added in quadrature. The total uncertainties are dominated by the uncertainty of the trigger correction, which is currently probably over estimated. Due to the limited scope of this thesis, a further investigation into the systematic uncertainty of the trigger correction was not possible. This may be improved in the future (see chapter 10).

Source	$\frac{D^0\to K^-\pi^+\pi^-\pi^+}{D^0\to K^-\pi^+e^-e^+}$	
	brem0	**brem1+**
Material interactions	2.0%	
Tracking maps	1.6%	
PID smearing kernel	2.7%	0.94%
Trigger weights	27%	28%
MC sample sizes	2.8%	2.4%
Total	27%	28%

Table 8.4: Mayor relative systematic uncertainties.

9 Branching Fraction Determination

The branching fraction for $D^0 \to K^-\pi^+e^-e^+$ is calculated using the event yields determined in chapter 6 and the efficiencies from chapter 7 for both signal and normalization channel. Since the yields and efficiencies for the signal channel are evaluated separately for both bremsstrahlung categories, the formula for the branching fraction in equation 4.2 is slightly modified:

$$\mathcal{B}_{D^0\to K^-\pi^+e^-e^+} = \mathcal{B}_{D^0\to K^-\pi^+\pi^-\pi^+}\cdot\left(\frac{N^{brem0}_{D^0\to K^-\pi^+e^-e^+}}{\epsilon^{brem0}_{D^0\to K^-\pi^+e^-e^+}} + \frac{N^{brem1+}_{D^0\to K^-\pi^+e^-e^+}}{\epsilon^{brem1+}_{D^0\to K^-\pi^+e^-e^+}}\right)\cdot\frac{\epsilon_{D^0\to K^-\pi^+\pi^-\pi^+}}{N_{D^0\to K^-\pi^+\pi^-\pi^+}}. \tag{9.1}$$

Inserting the yields and efficiencies into this formula results to:

$$\mathcal{B}_{D^0\to K^-\pi^+[e^-e^+]_{\rho^0,\omega}} = (3.6\pm0.2(\text{stat.})\pm0.7(\text{sys.},\epsilon)\pm0.06(\mathcal{B}_{D^0\to K^-\pi^+\pi^-\pi^+}))\times10^{-6}. \tag{9.2}$$

The statistical uncertainty is given by the statistical errors of the event yields. The systematic uncertainty is calculated by the uncertainties of the efficiencies. A summary of all systematic uncertainties can be found in table 8.4. The third uncertainty given in equation 9.2 is due to the measurement of the branching fraction for the normalization channel ($\mathcal{B}_{D^0\to K^-\pi^+\pi^-\pi^+}$). As this is an external input to the analysis, it is also a systematic uncertainty. Systematic and statistical uncertainties are assumed to be independent from each other and are added in quadrature. This results in:

$$\mathcal{B}_{D^0\to K^-\pi^+[e^-e^+]_{\rho^0,\omega}} = (3.6\pm0.8)\times10^{-6}. \tag{9.3}$$

10 Conclusion

This thesis presents the branching fraction measurement of the semi-leptonic charm decay $D^0 \to K^-\pi^+e^-e^+$ with proton-proton collision data collected by the LHCb experiment in 2017 and 2018, corresponding to an integrated luminosity of $3.8\,\mathrm{fb}^{-1}$. The kinematic range of the invariant mass of the electron pair is restricted to a window around the masses of the ρ^0 and ω mesons: $675\,\mathrm{MeV}/c^2 < m(ee) < 875\,\mathrm{MeV}/c^2$. The branching fraction measurement was performed relative to the normalization decay channel $D^0 \to K^-\pi^+\pi^-\pi^+$.

The previous chapters outlined how data samples with decay candidates for the signal and normalization channel are obtained. In the selection, the samples are filtered to reduce the amount of background contamination. This is done by defining trigger requirements and imposing cuts on kinematic, topological and particle identification variables. The data sample of the signal channel is split into two categories, depending on whether or not bremsstrahlung photons were added to the decay candidates. The number of signal and normalization channel candidates is determined by fits to the D^0 meson mass distributions. Corresponding simulated samples are used to determine fit models. Additionally, they are used to calculate reconstruction and selection efficiencies. The differences between simulation and data in tracking, particle identification and trigger response are corrected by data-driven methods. This is done with calibration samples from other decays. The systematic uncertainties arising from the finite MC sample sizes and the efficiency corrections are studied. The largest single systematic effect stems from the correction of the trigger efficiency. The resulting value for the branching fraction is:

$$\mathcal{B}_{D^0\to K^-\pi^+[e^-e^+]_{\rho^0,\omega}} = (3.6 \pm 0.2 \pm 0.7 \pm 0.06) \times 10^{-6}, \tag{10.1}$$

where first uncertainty is statistical, the second is systematic and the third is due to the uncertainty of the branching fraction of the normalization channel. The result is in agreement (1σ) to the previous measurement performed by the BaBar collaboration [16]:

$$\mathcal{B}_{D^0\to K^-\pi^+[e^-e^+]_{\rho^0,\omega}} = (4.0 \pm 0.5 \pm 0.2 \pm 0.1) \times 10^{-6}, \tag{10.2}$$

which has a much smaller systematic uncertainty.

For a future publication of the results of this analysis, further aspects have to be studied. The uncertainty for the trigger correction is currently probably overestimated. By statistical methods such as bootstrapping, the trigger correction could

be repeatedly evaluated. The resulting variation of the corrected trigger efficiencies would be a more accurate estimate of the systematic uncertainty. Furthermore, a more advanced trigger strategy allowing a more precise description of the trigger efficiency could be used for the analysis. This could be achieved by defining two mutually exclusive samples; one containing TIS events, the other one containing TOS events that are not already in the first sample, as it was done by [49, 50]. For the TIS events, the trigger decision does not depend on the signal. Thus, all correction factors for the trigger efficiency correction of the TIS events could be obtained from the statistically larger $B^0 \to (K^* \to) K^+\pi^-(J/\psi \to)\mu^+\mu^-$ samples. This would then decrease the systematic uncertainty of the trigger correction for the TIS sample. For the reconstruction and acceptance efficiencies, the signal MC sample can not be divided into the two bremsstrahlung categories. Therefore, possible differences between data and MC in the fraction of candidates, for which bremsstrahlung photons are added, are neglected. Another systematic uncertainty, which was not studied in this thesis, is the impact of the cut on the invariant mass of the electrons. Due to energy resolution effects in the electron reconstruction, bin migration occurs. This influences the number of candidates inside and outside the cut range. Furthermore, crosschecks for the fitting procedure need to be done. Firstly, toy studies need to be performed to confirm that the fits are not biased. Pseudo-data would be generated according to the mass distributions of signal and normalization channel where the event count is fluctuated by a Poisson distribution. This data needs to be fitted with the same models to check the stability of the result. In a second step, more detailed background studies need to be performed. In this thesis, only background from $D^0 \to K^-\pi^+\pi^-\pi^+$ decays and combinatorial background are assumed.

Currently, the data taking period for LHC Run 3 has started. The newly upgraded LHCb detector is capable to go to higher luminosities with further upgrades planned in the future. Including Run 3 data, the statistical uncertainty on the branching fraction measurement should scale with the inverse of the square root of the Luminosity increase.

With an increased data set, the next step would be to perform a measurement in other kinematic regions for the electron pair. This way, a total branching fraction for $D^0 \to K^-\pi^+e^-e^+$ could be determined and tests of lepton flavor universality could be performed using branching fraction measurements of the decay $D^0 \to K^-\pi^+\mu^-\mu^+$.

Bibliography

[1] G. Aad et al. Observation of a new particle in the search for the standard model higgs boson with the ATLAS detector at the LHC. *Physics Letters B*, 716(1):1–29, sep 2012. doi: 10.1016/j.physletb.2012.08.020. URL `https://doi.org/10.1016%2Fj.physletb.2012.08.020`.

[2] S. Chatrchyan et al. Observation of a new boson at a mass of 125 GeV with the CMS experiment at the LHC. *Physics Letters B*, 716(1):30–61, sep 2012. doi: 10.1016/j.physletb.2012.08.021. URL `https://doi.org/10.1016%2Fj.physletb.2012.08.021`.

[3] Dominik Mitzel. *Search for new physics in rare four-body charm decays*. PhD thesis, U. Heidelberg (main), 2019.

[4] R. Aaij et al. Observation of D^0 meson decays to $\pi^+\pi^-\mu^+\mu^-$ and $K^+K^-\mu^+\mu^-$ final states. *Phys. Rev. Lett.*, 119:181805, Oct 2017. doi: 10.1103/PhysRevLett.119.181805. URL `https://link.aps.org/doi/10.1103/PhysRevLett.119.181805`.

[5] Roel Aaij et al. Measurement of angular and CP asymmetries in $D^0 \to \pi^+\pi^-\mu^+\mu^-$ and $D^0 \to K^+K^-\mu^+\mu^-$ decays. *Phys. Rev. Lett.*, 121(9):091801, 2018. doi: 10.1103/PhysRevLett.121.091801. URL `http://cds.cern.ch/record/2627588`. All figures and tables, along with any supplementary material and additional information, are available at https://lhcbproject.web.cern.ch/lhcbproject/Publications/LHCbProjectPublic/LHCb-PAPER-2018-020.html.

[6] LHCb collaboration, I. Bediaga, et al. Physics case for an lhcb upgrade ii - opportunities in flavour physics, and beyond, in the hl-lhc era, 2019.

[7] Roel Aaij et al. First observation of the decay $D^0 \to K^-\pi^+\mu^+\mu^-$ in the ρ^0-ω region of the dimuon mass spectrum. *Phys. Lett. B*, 757:558, 2016. doi: 10.1016/j.physletb.2016.04.029. URL `https://cds.cern.ch/record/2063226`. 21 pages, 3 figures. All figures and tables, along with any supplementary material and additional information, are available at https://lhcbproject.web.cern.ch/lhcbproject/Publications/LHCbProjectPublic/LHCb-PAPER-2015-043.html.

[8] Mark Thomson. *Modern particle physics*. Cambridge University Press, New York, 2013. ISBN 978-1-107-03426-6. doi: 10.1017/CBO9781139525367.

[9] Wikimedia Commons. File:standard model of elementary particles.svg — wikimedia commons, the free media repository, 2023. URL https://commons.wikimedia.org/w/index.php?title=File:Standard_Model_of_Elementary_Particles.svg&oldid=746153035. [Online; accessed 3-April-2023].

[10] E. Noether. Invariante variationsprobleme. *Nachrichten von der Gesellschaft der Wissenschaften zu Göttingen, Mathematisch-Physikalische Klasse*, 1918: 235–257, 1918. URL http://eudml.org/doc/59024.

[11] LHCb collaboration. First observation of a doubly charged tetraquark and its neutral partner, 2022.

[12] LHCb collaboration. Observation of a $j/\psi\lambda$ resonance consistent with a strange pentaquark candidate in $b^- \to j/\psi\lambda\bar{p}$ decays, 2022.

[13] Makoto Kobayashi and Toshihide Maskawa. CP-Violation in the Renormalizable Theory of Weak Interaction. *Progress of Theoretical Physics*, 49 (2):652–657, 02 1973. ISSN 0033-068X. doi: 10.1143/PTP.49.652. URL https://doi.org/10.1143/PTP.49.652.

[14] Lincoln Wolfenstein. Parametrization of the kobayashi-maskawa matrix. *Phys. Rev. Lett.*, 51:1945–1947, Nov 1983. doi: 10.1103/PhysRevLett.51.1945. URL https://link.aps.org/doi/10.1103/PhysRevLett.51.1945.

[15] Luigi Cappiello, Oscar Cata, and Giancarlo D'Ambrosio. Standard Model prediction and new physics tests for $D^0 \to h^+h^-\ell^+\ell^-(h = \pi, K : \ell = e, \mu)$. *JHEP*, 04:135, 2013. doi: 10.1007/JHEP04(2013)135.

[16] J. P. Lees et al. Observation of the Decay $D^0 \to K^-\pi^+e^+e^-$. *Phys. Rev. Lett.*, 122(8):081802, 2019. doi: 10.1103/PhysRevLett.122.081802.

[17] Lyndon Evans and Philip Bryant. Lhc machine. *Journal of Instrumentation*, 3(08):S08001, aug 2008. doi: 10.1088/1748-0221/3/08/S08001. URL https://dx.doi.org/10.1088/1748-0221/3/08/S08001.

[18] A Augusto Alves Jr et al. The lhcb detector at the lhc. *Journal of Instrumentation*, 3(08):S08005, aug 2008. doi: 10.1088/1748-0221/3/08/S08005. URL https://dx.doi.org/10.1088/1748-0221/3/08/S08005.

[19] Rolf Lindner. LHCb layout 2. LHCb schema 2. LHCb Collection., 2008. URL https://cds.cern.ch/record/1087860.

[20] Wander Baldini, J Blouw, S Blusk, N Gilardi, Olivier Deschamps, Florin Maciuc, Jacopo Nardulli, A Papanestis, C Parkes, Seb Viret, M Needham, J Tilburg, S Vecchi, and K Vervink. Overview of lhcb alignment. *Proceedings of the 1st LHC Detector Alignment Workshop*, 01 2007.

[21] M. Adinolfi et al. Performance of the LHCb RICH detector at the LHC. *The European Physical Journal C*, 73(5), may 2013. doi: 10.1140/epjc/s10052-013-2431-9. URL https://doi.org/10.1140%2Fepjc%2Fs10052-013-2431-9.

[22] Jonathan Robert Harrison. *Radiation damage studies in the LHCb VELO detector and searches for lepton flavour and baryon number violating tau decays*. PhD thesis, Manchester U., 2014. URL https://cds.cern.ch/record/1712972. Presented 16 05 2014.

[23] LHCb detector performance. *International Journal of Modern Physics A*, 30 (07):1530022, mar 2015. doi: 10.1142/s0217751x15300227. URL https://doi.org/10.1142%2Fs0217751x15300227.

[24] S Tolk, J Albrecht, F Dettori, and A Pellegrino. Data driven trigger efficiency determination at LHCb. Technical report, CERN, Geneva, 2014. URL https://cds.cern.ch/record/1701134.

[25] Roel Aaij et al. Design and performance of the LHCb trigger and full real-time reconstruction in Run 2 of the LHC. *JINST*, 14(04):P04013, 2019. doi: 10.1088/1748-0221/14/04/P04013. URL https://cds.cern.ch/record/2652801. 46 pages, 35 figures, 1 table. All figures and tables are available at https://cern.ch/lhcbproject/Publications/LHCbProjectPublic/LHCb-DP-2019-001.html.

[26] S Miglioranzi, M Clemencic, C Corti, S Easo, C R Jones, M Pappagallo, and P Robbe. The LHCb Simulation Application, Gauss: Design, Evolution and Experience. Technical report, CERN, Geneva, 2011. URL https://cds.cern.ch/record/1322402.

[27] Torbjörn Sjöstrand, Stephen Mrenna, and Peter Skands. A brief introduction to PYTHIA 8.1. *Computer Physics Communications*, 178(11):852–867, jun 2008. doi: 10.1016/j.cpc.2008.01.036. URL https://doi.org/10.1016%2Fj.cpc.2008.01.036.

[28] D. J. Lange. The EvtGen particle decay simulation package. *Nucl. Instrum. Meth. A*, 462:152–155, 2001. doi: 10.1016/S0168-9002(01)00089-4.

[29] S. Agostinelli et al. GEANT4–a simulation toolkit. *Nucl. Instrum. Meth. A*, 506:250–303, 2003. doi: 10.1016/S0168-9002(03)01368-8.

[30] The boole project. https://lhcbdoc.web.cern.ch/lhcbdoc/boole/. Accessed: 2023.

[31] The moore project. https://lhcbdoc.web.cern.ch/lhcbdoc/moore/. Accessed: 2023.

[32] The brunel project. https://lhcbdoc.web.cern.ch/lhcbdoc/brunel/. Accessed: 2023.

[33] The davinci project. https://lhcbdoc.web.cern.ch/lhcbdoc/davinci/. Accessed: 2023.

[34] R Brun, F Rademakers, and S Panacek. ROOT, an object oriented data analysis framework. 2000. URL https://cds.cern.ch/record/491486.

[35] Lhcb starterkit lessons: Changes to the data flow in run 2. https://lhcb.github.io/starterkit-lessons/first-analysis-steps/run-2-data-flow.html. Accessed: 2023.

[36] Pankaj Mehta, Marin Bukov, Ching-Hao Wang, Alexandre G.R. Day, Clint Richardson, Charles K. Fisher, and David J. Schwab. A high-bias, low-variance introduction to machine learning for physicists. *Physics Reports*, 810:1–124, may 2019. doi: 10.1016/j.physrep.2019.03.001. URL https://doi.org/10.1016%2Fj.physrep.2019.03.001.

[37] Alan S. Cornell, Wesley Doorsamy, Benjamin Fuks, Gerhard Harmsen, and Lara Mason. Boosted decision trees in the era of new physics: a smuon analysis case study. *Journal of High Energy Physics*, 2022(4), apr 2022. doi: 10.1007/jhep04(2022)015. URL https://doi.org/10.1007%2Fjhep04%282022%29015.

[38] Lhcb starterkit lessons: Tistos diy. https://lhcb.github.io/starterkit-lessons/second-analysis-steps/tistos-diy.html. Accessed: 2023.

[39] S. Dobbs et al. Measurement of absolute hadronic branching fractions of D mesons and e+ e- —> D anti-D cross-sections at the psi(3770). *Phys. Rev. D*, 76:112001, 2007. doi: 10.1103/PhysRevD.76.112001.

[40] Q. He et al. Measurement of absolute hadronic branching fractions of D mesons and e+ e- —> D anti-D cross sections at E(cm) = 3773-MeV. *Phys. Rev. Lett.*, 95:121801, 2005. doi: 10.1103/PhysRevLett.95.121801. [Erratum: Phys.Rev.Lett. 96, 199903 (2006)].

[41] H. Albrecht et al. A Study of anti-B0 —> D*+ lepton- anti-neutrino and B0 anti-B0 mixing using partial D*+ reconstruction. *Phys. Lett. B*, 324:249–254, 1994. doi: 10.1016/0370-2693(94)90415-4.

[42] R. L. Workman et al. Review of Particle Physics. *PTEP*, 2022:083C01, 2022. doi: 10.1093/ptep/ptac097.

[43] Derkach, Denis, Hushchyn, Mikhail, and Kazeev, Nikita. Machine learning based global particle identification algorithms at the lhcb experiment. *EPJ Web Conf.*, 214:06011, 2019. doi: 10.1051/epjconf/201921406011. URL https://doi.org/10.1051/epjconf/201921406011.

[44] Andreas Hocker et al. TMVA - Toolkit for Multivariate Data Analysis. 3 2007.

[45] R. Nobrega, E Marinari, G. Penso, and Davide Pinci. Development of the experiment control system and performance study of the muon chambers for the lhcb experiment. 05 2023.

[46] Fabian Linsenmeier. Measurement of the branching fraction for $D^0 \to K^-\pi^+[e^+e^-]_{\rho,\omega}$. Bachelor's thesis, U. Heidelberg, 2022.

[47] Tomasz Skwarnicki. *A study of the radiative CASCADE transitions between the Upsilon-Prime and Upsilon resonances*. PhD thesis, Cracow, INP, 1986.

[48] P. L. Chebyshev. *Théorie Des Mécanismes Connus Sous Le Nom De Parallélogrammes*. St.-Pétersbourg: Imprimerie de l'Académie impériale des sciences, 1853.

[49] Test of lepton universality in $b \to s\ell^+\ell^-$ decays. Technical report, CERN, Geneva, 2022. URL `https://cds.cern.ch/record/2845047`. All figures and tables, along with any supplementary material and additional information, are available at https://cern.ch/lhcbproject/Publications/p/LHCb-PAPER-2022-046.html (LHCb public pages).

[50] Measurement of lepton universality parameters in $B^+ \to K^+\ell^+\ell^-$ and $B^0 \to K^{*0}\ell^+\ell^-$ decays. Technical report, CERN, Geneva, 2022. URL `https://cds.cern.ch/record/2845040`. All figures and tables, along with any supplementary material and additional information, are available at https://cern.ch/lhcbproject/Publications/p/LHCb-PAPER-2022-045.html (LHCb public pages).

[51] A. Poluektov. Correction of simulated particle identification response in LHCb using transformation of variables. Technical report, CERN, Geneva, 2017.

[52] Lucio Anderlini et al. The PIDCalib package. Technical report, CERN, Geneva, 2016. URL `https://cds.cern.ch/record/2202412`.

[53] Michel De Cian. *Track Reconstruction Efficiency and Analysis of $B^0 \to K^{*0}\mu^+\mu^-$ at the LHCb Experiment*. PhD thesis, Zurich U., 2013. URL `https://cds.cern.ch/record/1605179`. Presented 14 Mar 2013.

[54] Michel De Cian, Stephanie Hansmann-Menzemer, Andreas Jaeger, Paul Seyfert, Jeroen van Tilburg, and Sebastian Wandernoth. Measurement of the track finding efficiency. Technical report, CERN, Geneva, 2012. URL `https://cds.cern.ch/record/1402577`.

[55] B. Efron. Bootstrap Methods: Another Look at the Jackknife. *The Annals of Statistics*, 7(1):1 – 26, 1979. doi: 10.1214/aos/1176344552. URL `https://doi.org/10.1214/aos/1176344552`.

A Appendix

In the following, the remaining correction factors used for the correction of the trigger efficiency are given.

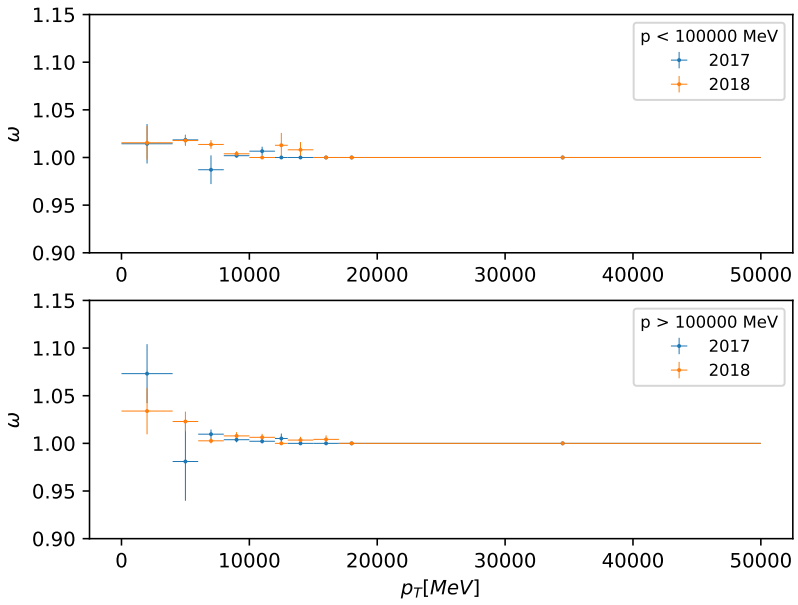

Figure A.1: Trigger correction factors in kinematic bins of p_T and p for the HLT1 trigger calculated with $B^0 \to (K^* \to) K^+\pi^-(J/\psi \to) e^+e^-$ decays. The factors for the lower momentum bin is shown in the upper plots, the factors for the upper momentum bin are in the lower plots, respectively. The different years of data-taking are shown in different colors.

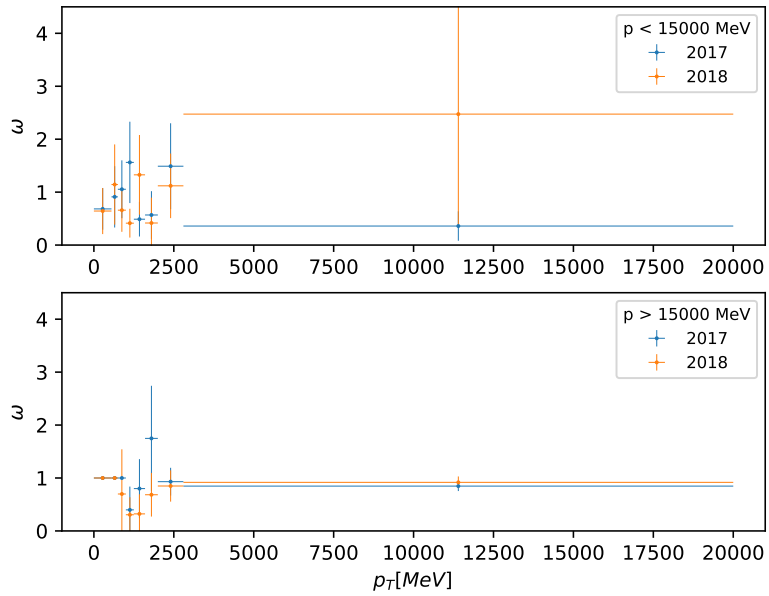

(a) $B^0 \to K^+\pi^-e^+e^-$ decays

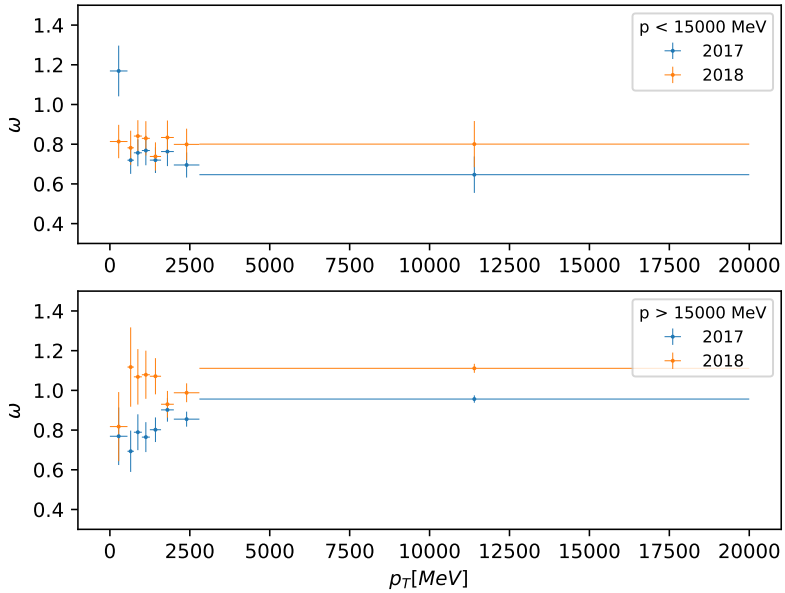

(b) $B^0 \to K^+\pi^-\mu^+\mu^-$ decays

Figure A.2: L0 Trigger correction factors for pions calculated with $B^0 \to (K^* \to)K^+\pi^-(J/\psi \to)e^+e^-$ decays (top) and $B^0 \to (K^* \to)K^+\pi^-(J/\psi \to)\mu^+\mu^-$ decays (bottom). The factors are given in kinematic bins of p_T and p. The factors for the lower momentum bin is shown in the upper plots, the factors for the upper momentum bin are in the lower plots, respectively. The different years of data-taking are shown in different colors.

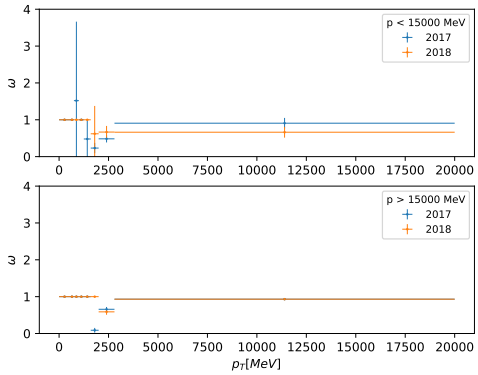

(a) Electron$_1$: **brem0**

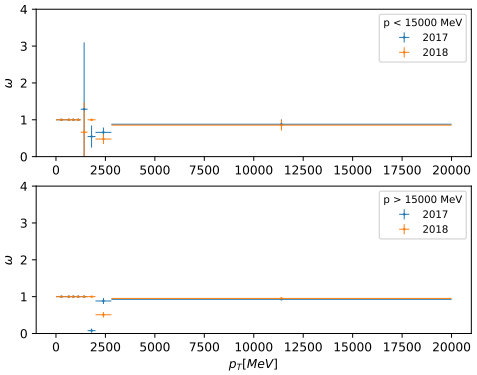

(b) Electron$_2$: **brem0**

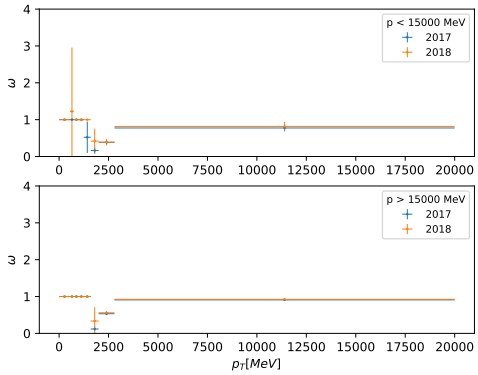

(c) Electron$_1$: **brem1**+

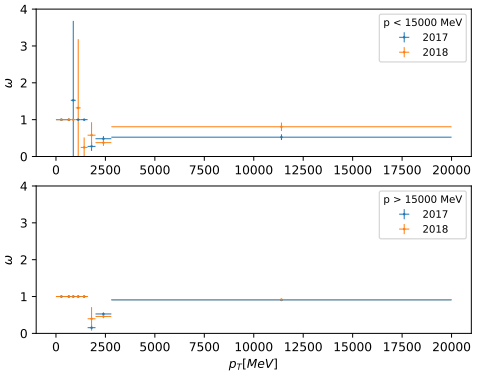

(d) Electron$_2$: **brem1**+

Figure A.3: Trigger correction factors in kinematic bins of p_T and p for electrons calculated with $B^0 \to (K^* \to) K^+\pi^-(J/\psi \to) e^+e^-$ decays. The subfigures (a) and (b) show the factors for the electrons with no added bremsstrahlung. The subfigures (c) and (d) show the factors for the electrons with one or more added photons. The factors for the lower momentum bin is shown in the upper plots, the factors for the upper momentum bin are in the lower plots, respectively. The different years of data-taking are shown in different colors.

Acknowledgements

I would like to express my gratitude to those who have supported me during my work on this master thesis. First, I would like to thank Prof. Ulrich Uwer, who gave me the opportunity to join the LHCb collaboration to carry out this analysis at the Physikalisches Institut Heidelberg and provided me with helpful feedback. I would also like to thank Prof. Klaus Reygers for making himself available as a second referee.
My special thanks go to Daniel Unverzagt for his time and patience in discussing the smaller and bigger questions that arose during my work. He guided me through the analysis and always had time to address problems or to figure out the next steps. I would also like to thank Dr. Martino Borsato for his feedback and helpful explanations of the intricacies of the LHCb detector. I am grateful for the whole LHCb Heidelberg group, not only for welcoming me into the group and helping me out with my questions, but also for the fun activities on weekends or holidays outside of the institute.
Finally, I would like to thank my family for supporting and encouraging me throughout my studies. This would not have been possible without you.

Erklärung:

Ich versichere, dass ich diese Arbeit selbstständig verfasst habe und keine anderen als die angegebenen Quellen und Hilfsmittel benutzt habe.

Heidelberg, den 31.05.2023 .....